RESEARCH ARTICLE

Proteomic Screens for Suppressors of Anoikis Identify IL1RAP as a Promising Surface Target in Ewing Sarcoma

Hai-Feng Zhang[1,2], Christopher S. Hughes[1,2], Wei Li[3], Jian-Zhong He[4], Didier Surdez[5,6], Amal M. El-Naggar[1,2], Hongwei Cheng[2,7], Anna Prudova[2,8], Alberto Delaidelli[1,2], Gian Luca Negri[8], Xiaojun Li[2], Maj Sofie Ørum-Madsen[9], Michael M. Lizardo[2], Htoo Zarni Oo[9], Shane Colborne[8], Taras Shyp[1,2], Renata Scopim-Ribeiro[1,2], Colin A. Hammond[10], Anne-Chloe Dhez[1,2], Sofya Langman[1,2], Jonathan K.M. Lim[1,2], Sonia H.Y. Kung[9], Amy Li[1,2], Anne Steino[2], Mads Daugaard[9,11], Seth J. Parker[12,13], Ramon I. Klein Geltink[1,12], Rimas J. Orentas[14,15], Li-Yan Xu[4], Gregg B. Morin[8,16], Olivier Delattre[5], Dimiter S. Dimitrov[3], and Poul H. Sorensen[1,2]

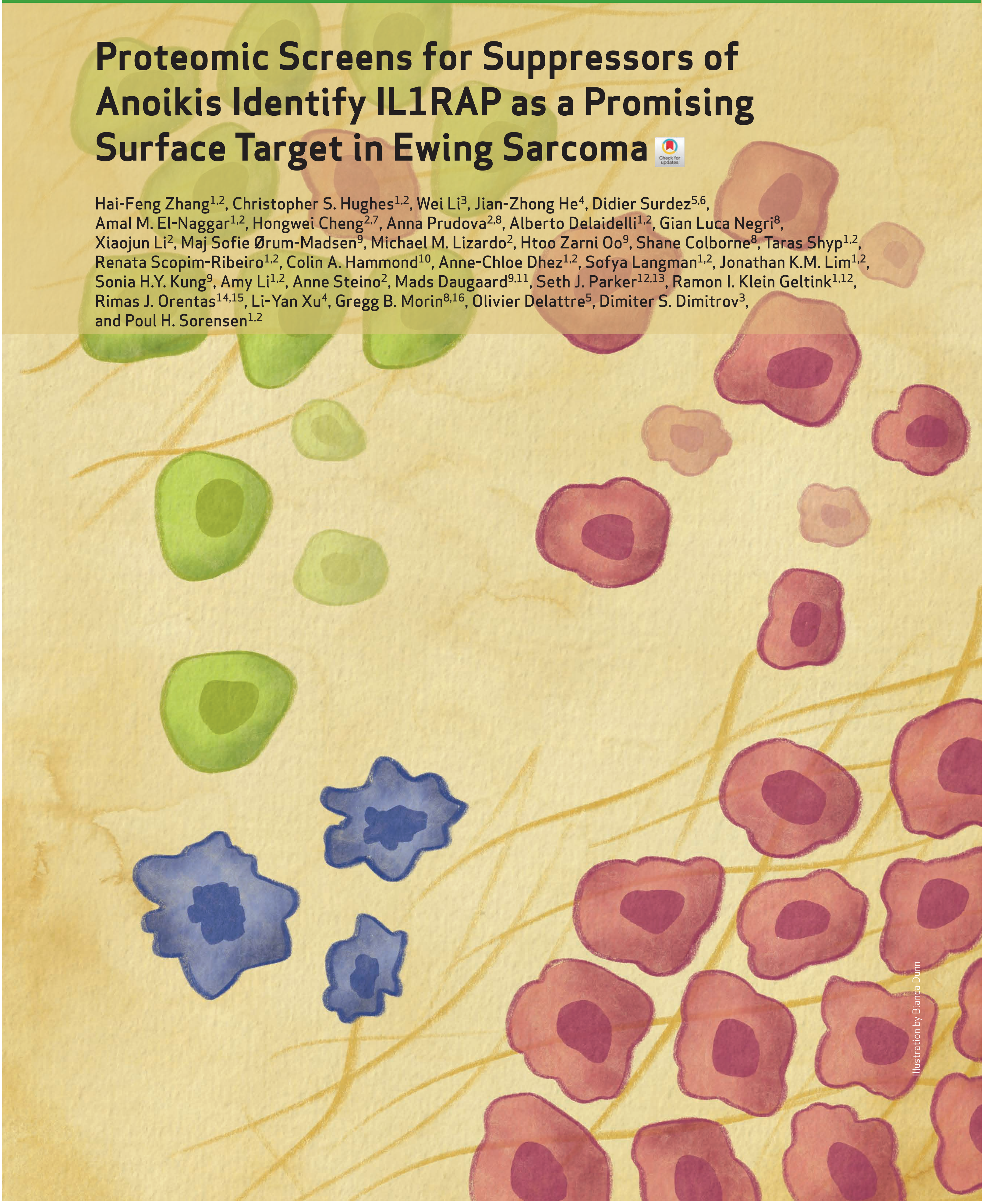

Illustration by Bianca Dunn

ABSTRACT

Cancer cells must overcome anoikis (detachment-induced death) to successfully metastasize. Using proteomic screens, we found that distinct oncoproteins upregulate IL1 receptor accessory protein (IL1RAP) to suppress anoikis. IL1RAP is directly induced by oncogenic fusions of Ewing sarcoma, a highly metastatic childhood sarcoma. IL1RAP inactivation triggers anoikis and impedes metastatic dissemination of Ewing sarcoma cells. Mechanistically, IL1RAP binds the cell-surface system X_c^- transporter to enhance exogenous cystine uptake, thereby replenishing cysteine and the glutathione antioxidant. Under cystine depletion, IL1RAP induces cystathionine gamma lyase (CTH) to activate the transsulfuration pathway for *de novo* cysteine synthesis. Therefore, IL1RAP maintains cyst(e)ine and glutathione pools, which are vital for redox homeostasis and anoikis resistance. IL1RAP is minimally expressed in pediatric and adult normal tissues, and human anti-IL1RAP antibodies induce potent antibody-dependent cellular cytotoxicity of Ewing sarcoma cells. Therefore, we define IL1RAP as a new cell-surface target in Ewing sarcoma, which is potentially exploitable for immunotherapy.

SIGNIFICANCE: Here, we identify cell-surface protein IL1RAP as a key driver of metastasis in Ewing sarcoma, a highly aggressive childhood sarcoma. Minimal expression in pediatric and adult normal tissues nominates IL1RAP as a promising target for immunotherapy.

See related commentary by Yoon and DeNicola, p. 2679.

INTRODUCTION

Metastasis is responsible for up to 90% of cancer-related deaths, representing the leading cause of cancer-associated mortality (1). Despite extensive research into this process, reducing metastasis-associated mortality remains a major clinical unmet need (2), and identification of key drivers of metastasis carries paramount significance. Ewing sarcoma is the second most common bone cancer in children and adolescents, and metastatic status at diagnosis remains the strongest prognostic factor across various standard-of-care treatments (3). Ewing sarcoma patients with metastatic disease have a <30% overall survival rate, which has not improved for decades (3).

In the metastatic cascade, a major obstacle that disseminated tumor cells must overcome is anoikis (4), or cell death induced by loss of attachment to the extracellular matrix (ECM). Genes that promote resistance to anoikis can confer enhanced metastatic capacity (4, 5). Delineation of novel anoikis resistance factors will open new avenues for designing effective therapies to block metastasis. However, most *in vitro* studies have historically used conventional two-dimensional (2-D) cultures to identify regulators of cancer growth (6–8), hindering the identification of important anoikis regulators. Therefore, in this study we utilized 3-D cultures of tumor cells to model anoikis stress (9) as a means to identify novel antianoikis and prometastatic signatures.

The tripeptide metabolite glutathione (GSH) is a key antioxidant in mammalian cells, and its availability represents a major determinant of cellular redox homeostasis (10, 11). GSH depletion results in accumulation of reactive oxygen species (ROS) as well as oxidized membrane phospholipids (known as lipid ROS), which may induce cell death, including anoikis (4, 12, 13) and ferroptosis (i.e., iron-dependent cell death; refs. 14–16). The rate-limiting substrate for GSH synthesis is cysteine, which cells acquire from exogenous cystine uptake via the xCT/CD98 transporter (also known as system X_c^-), or *de novo* synthesis via the transsulfuration (TSS) pathway that converts serine and methionine to cysteine (10, 11, 17, 18). Upon extracellular cystine depletion or xCT blockade, cells can switch to the TSS pathway to maintain cysteine pools and cell survival (18). Despite the critical role of cysteine for metabolic and redox homeostasis in cancer

---

[1]Department of Pathology and Laboratory Medicine, University of British Columbia, Vancouver, British Columbia, Canada. [2]Department of Molecular Oncology, BC Cancer Agency, Vancouver, British Columbia, Canada. [3]Center for Antibody Therapeutics, Division of Infectious Diseases, Department of Medicine, University of Pittsburgh Medical School, Pittsburgh, Pennsylvania. [4]Institute of Oncologic Pathology, Shantou University Medical College, Shantou, Guangdong, China. [5]INSERM U830, Equipe Labellisée LNCC, Diversity and Plasticity of Childhood Tumors Lab, PSL Research University, SIREDO Oncology Centre, Institut Curie Research Centre, 75005 Paris, France. [6]Balgrist University Hospital, University of Zurich, Zurich, Switzerland. [7]Modelling and Translation Laboratory, Xinxiang Medical University, Xinxiang, Henan, China. [8]Canada's Michael Smith Genome Sciences Centre, Vancouver, British Columbia, Canada. [9]Vancouver Prostate Centre, Vancouver, British Columbia, Canada. [10]Terry Fox Laboratory, British Columbia Cancer Agency, Vancouver, British Columbia, Canada. [11]Department of Urologic Sciences, University of British Columbia, British Columbia, Canada. [12]BC Children's Hospital Research Institute, Vancouver, British Columbia, Canada. [13]Department of Biochemistry & Molecular Biology, University of British Columbia, Vancouver, British Columbia, Canada. [14]Seattle Children's Research Institute, Seattle, Washington. [15]Department of Pediatrics, University of Washington School of Medicine, Seattle, Washington. [16]Department of Medical Genetics, University of British Columbia, Vancouver, British Columbia, Canada.

Current address for J.K.M. Lim: Department of Neuropathology, Medical Faculty, Heinrich Heine University, Düsseldorf, Germany.

O. Delattre and D.S. Dimitrov contributed equally to this article.

Corresponding Author: Poul H. Sorensen, Department of Molecular Oncology, British Columbia Cancer Research Centre, 675 West 10th Avenue, Vancouver, BC V5Z1L3, Canada. Phone: 604-675-8202; E-mail: psor@mail.ubc.ca

Cancer Discov 2021;11:2884–903

doi: 10.1158/2159-8290.CD-20-1690

cells (10, 11), how these two processes are balanced to meet the high demand for cysteine remains elusive, such as in cancer cells with low expression of xCT (19, 20) or via key enzymes for TSS such as cystathionine β-synthase (CBS; ref. 18). A better understanding of specific factors that mediate the interplay between cystine uptake and the TSS for cysteine replenishment may elucidate novel approaches to block cysteine metabolism and therefore ROS homeostasis in cancer cells.

In this report, we utilized combined proteomic and translatomic screens in 3-D cultures to identify factors that mitigate anoikis in fibroblasts transformed by distinct oncoproteins. This approach identified IL1RAP as a previously unknown suppressor of anoikis and an important regulator of redox homeostasis in transformed cells. IL1RAP is a cell-surface protein known to associate with IL1 receptors (IL1R), functioning as an IL1R coreceptor to mediate IL1 family cytokine signaling pathways in immune cells, e.g., T lymphocytes and mast cells (21). IL1RAP was previously shown to have protumorigenic roles in myeloid leukemias (22–25), whereas its role in other cancers is unknown. Instead, we found that in Ewing sarcoma, a highly metastatic childhood sarcoma, EWS–FLI1 and EWS–ERG fusion oncoproteins characteristic of this malignancy directly induce IL1RAP expression to activate both the system X_c^- transporter and the TSS pathway, but independently from IL1R. This unexpected function of IL1RAP confers Ewing sarcoma cells with the ability to maintain and replenish cysteine and GSH pools even when extracellular cystine uptake is limited, which is exploited as a cytoprotective mechanism during the metastatic cascade. From a therapeutic perspective, strong surface expression in cancers and minimal expression in normal tissues nominates IL1RAP as a promising immunotherapy target.

RESULTS

Identification of Novel Anoikis Suppressors in Oncogene-Transformed Mesenchymal Cells

Suppression of anoikis is well documented to play a critical role in metastasis, particularly in epithelial malignancies (4). To identify novel metastasis regulators in sarcomas, malignancies of the mesenchymal origin that are characterized by high metastatic rates (3), we first explored anoikis regulation in transformed mesenchymal cells. We used anchorage-independent growth in soft-agar and 3-D suspension cultures to model the anoikis phenotype (9) in NIH3T3 fibroblasts transformed with either KRAS^{G12V} or the ETV6–NTRK3 (EN) oncogenic tyrosine kinase, compared with nontransformed control cells (MSCV vector alone). Each transformed line acquired dramatic anoikis resistance phenotypes, whereas control cells were unable to survive under the same conditions (Fig. 1A and B). In contrast, no major differences in cell growth were observed under 2-D monolayer cultures (Supplementary Fig. S1A). By tracking the time course of cell death in 3-D cultures, we observed that nontransformed cells rapidly underwent anoikis within the first 9 hours, whereas transformed lines successfully adapted to detachment during this interval (Fig. 1C; Supplementary Fig. S1B). To understand mechanisms driving these differences, we next compared acute proteomic changes in transformed versus control cells during adaptation to anoikis stress (Fig. 1D). To this end, we used tandem mass tag (TMT)–based mass spectrometry to identify global proteomic differences (Fig. 1E and F), as well as stable isotope labeling with amino acids in cell culture (SILAC) combined with Click chemistry to identify differences in acute protein synthesis (Fig. 1G and H), in cells adapting to 3-D growth. Integrated analyses of both global and acute proteomic data sets revealed a set of 60 proteins that were commonly altered in both KRAS^{G12V} and EN transformed cell lines in response to cell detachment, including 31 upregulated (Fig. 1I) and 29 downregulated proteins shared across both transformed lines (Supplementary Fig. S1C). Among the eight most highly upregulated proteins and potential drivers of anoikis resistance, namely CAPG, CPE, GNAI2, Il1RAP, MYO1B, NRP2, PEG3, and SH3KBP1, each showed higher mRNA levels in one or both oncogene-transformed cells compared with nontransformed controls, suggesting transcriptional regulation (Supplementary Fig. S1D). We then tested effects of gene knockdown of these eight candidates and found that *Gnai2*, *Capg*, *Nrp2*, and *Il1rap* are each critical for soft-agar colony formation of both EN (Supplementary Fig. S1E and S1F) and KRAS^{G12V} transformed cells (Supplementary Fig. S1G), validating our approach for uncovering novel anoikis resistance factors.

IL1RAP Is Highly Expressed in Ewing Sarcoma and Promotes Anoikis Resistance and *In Vivo* Metastasis

Because cancer cell surface proteins can be directly targeted by immunotherapeutic strategies, such as antibody drug conjugates or chimeric antigen receptor (CAR) T cell approaches, we selected surface proteins NRP2 and IL1RAP among the above newly identified anoikis suppressors for further analysis. We first determined if NRP2 and IL1RAP are deregulated in human cancers, particularly in sarcomas. By assessing publicly available databases, NRP2 was not exceptionally higher in sarcomas compared with other malignancies. However, we unexpectedly found extremely high IL1RAP expression at both the mRNA and protein level in Ewing sarcoma, a highly metastatic bone and soft-tissue malignancy, compared with other human cancers (Fig. 2A; Supplementary Fig. S2A and S2B). IL1RAP is a cell-surface protein best known as a coreceptor for IL1R signaling (ref. 21; see below). We confirmed *in vivo* IL1RAP protein expression and, in particular, its plasma membrane localization, by IHC in both Ewing sarcoma patient samples and Ewing sarcoma xenografts in mice (Fig. 2B). By Western blotting, IL1RAP was highly expressed across a panel of Ewing sarcoma cell lines (Supplementary Fig. S2C), and surface expression could readily be detected by immunofluorescence (IF) using antibodies to IL1RAP (Fig. 2C). Moreover, *IL1RAP* expression was markedly increased in both Ewing sarcoma tumors and a panel of Ewing sarcoma cell lines compared with mesenchymal stem cells (MSC; Supplementary Fig. S2D and S2E), the proposed Ewing sarcoma cell of origin (26). High *IL1RAP* expression correlates with poor event-free survival in two separate Ewing sarcoma patient cohorts and in a third cohort of mixed sarcomas (Supplementary Fig. S2F). Together, these findings point to a potential role for IL1RAP in the pathobiology of Ewing sarcoma.

IL1RAP knockdown in Ewing sarcoma cells with two independent shRNAs did not affect cell proliferation in 2-D cultures (Supplementary Fig. S2G), but dramatically blocked growth in both 3-D and soft-agar cultures (Fig. 2D; Supplementary Fig. S2H), and triggered marked anoikis in 3-D cultures

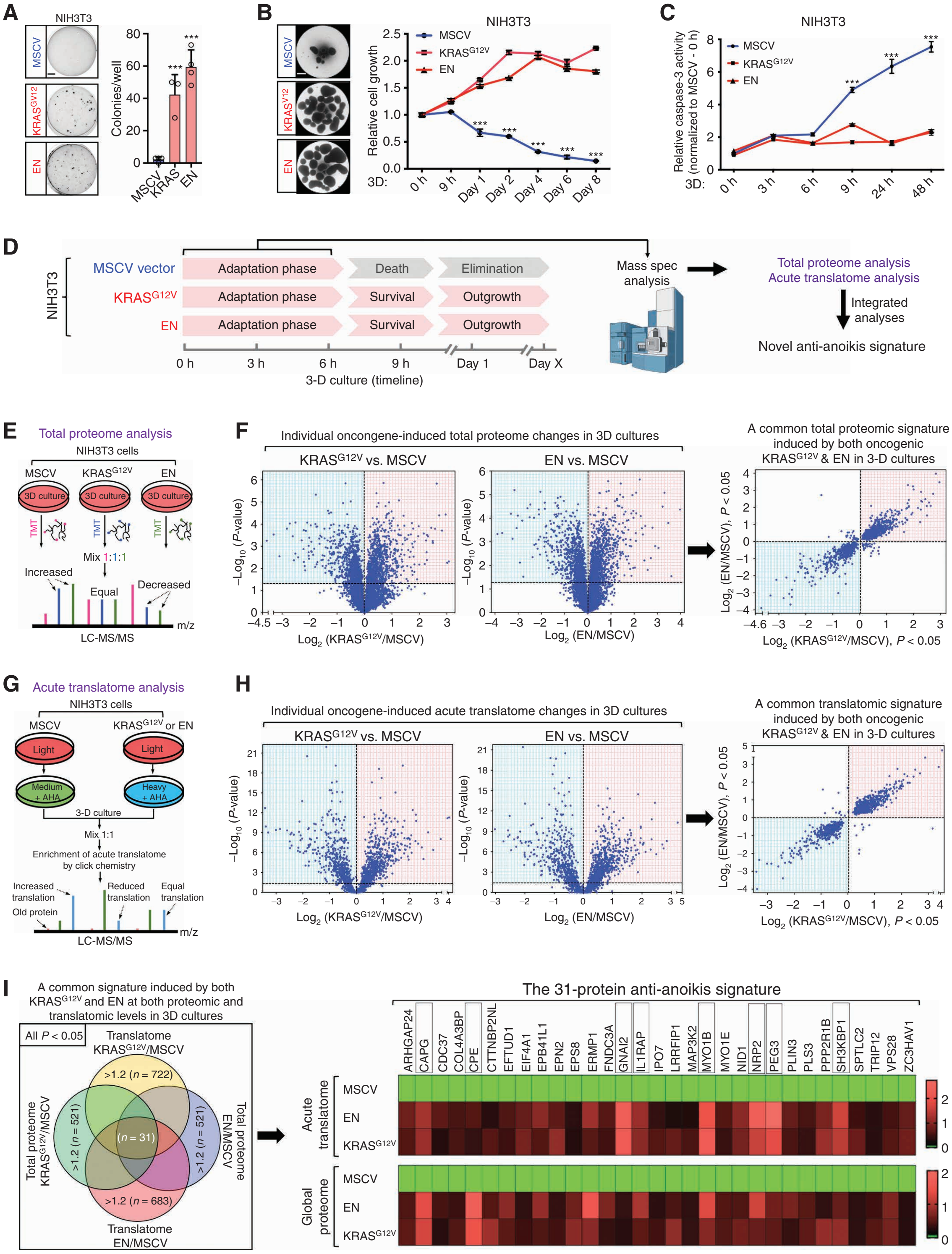

Figure 1. Identification of novel anoikis suppressors in oncogene-transformed fibroblasts. **A,** Soft-agar colony formation of NIH3T3 cells stably expressing MSCV vector control, oncogenic KRAS^{G12V}, or oncogenic ETV6–NTRK3 (EN). Scale bar, 5 mm. **B,** Spheroid growth of the indicated cells in 3-D cultures. Scale bar, 500 μm. **C,** Caspase-3 activity of the indicated cells grown in 3-D cultures. **D,** Schematic showing the strategies for identifying a novel signature regulating anoikis resistance. **E,** Schematic demonstrating the experimental design for global proteome analysis in cells cultured in 3-D conditions during the adaptation phase (0–6 hours). **F,** Global proteome changes induced by different oncogenes in NIH3T3 cells. **G,** Schematic demonstrating the experimental design for acute translatomic analysis in cells cultured in 3-D conditions during the adaptation phase (0–6 hours). **H,** Global acute translatomic changes induced by different oncogenes in NIH3T3 cells. **I,** Integrated analyses of the global proteomic and acute translatomic data sets shown in **F** and **H** identifies 31 upregulated proteins in response to detachment that were shared between KRAS^{G12V} and EN transformed cells compared with MSCV controls. For all panels, data, the mean±SD. Statistical significance was determined using unpaired two-tailed Student *t* test; ***, $P < 0.001$.

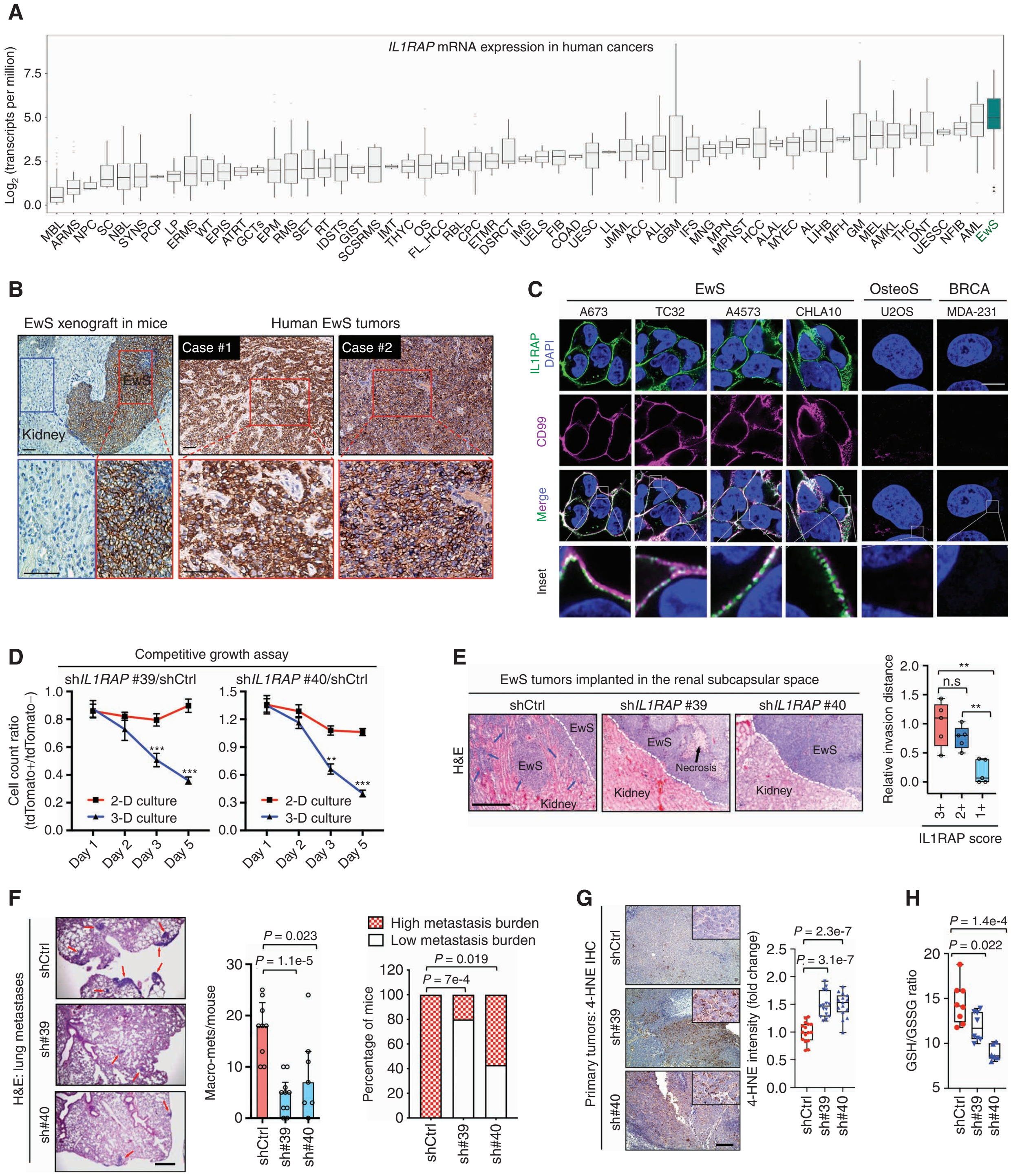

Figure 2. IL1RAP is highly expressed in Ewing sarcoma (EwS) and promotes anoikis resistance and *in vivo* metastasis. **A,** *IL1RAP* mRNA expression profile in human tumor samples. The plot is generated based on published RNA-sequencing data sets. **B,** IHC staining of IL1RAP in Ewing sarcoma (TC32) xenografts in mice and human Ewing sarcoma samples. Scale bars, 50 μm. **C,** IF staining of IL1RAP in the indicated cells analyzed by microscopy. Scale bar, 10 μm. **D,** Flow cytometry–based quantification of cell counts between TC32-sh*IL1RAP* (tdTomato+) and shCtrl cells cultured in 2-D or 3-D conditions. **E,** Left, hematoxylin and eosin (H&E) staining in TC32-derived xenografts implanted in the renal subcapsular space in mice. Dashed lines indicate the boundaries between Ewing sarcoma tumors and the surrounding kidney tissues, and blue arrows indicate the invasive Ewing sarcoma tumor cells. Scale bar, 100 μm. Right, quantification of local invasion distance by tumor cells with different IL1RAP staining intensities, $n = 7–10$. **F,** H&E staining of the lung sections and quantification of lung macrometastases and metastasis burden (see Methods); $n = 7–10$. **G,** IHC staining (left) and quantification (right) of 4-HNE staining intensity ($n = 15–16$ fields). Scale bar, 100 μm. **H,** GSH/GSSG ratios in the Ewing sarcoma xenografts derived from TC32 cells ($n = 6–8$). In **A**, data are presented as median values and the interquartile range. In **D**, data, means ± SD. In **E–G**, data, means ± SEM. In **H**, data, mean values and 10–90 percentile. Statistical significance was determined using unpaired two-tailed Student *t* test in all panels except the right panel of **F**. **, $P < 0.01$; ***, $P < 0.001$; n.s., no significance.

(Supplementary Fig. S2I). We next assessed effects of *IL1RAP* depletion *in vivo* using the murine renal subcapsular implantation model, previously utilized for evaluating Ewing sarcoma xenograft growth and spontaneous metastasis (5, 27, 28). We found that *IL1RAP* depletion moderately but significantly reduced primary tumor growth at primary implantation sites (Supplementary Fig. S2J). Moreover, primary tumors with *IL1RAP* knockdown displayed reduced invasiveness into adjacent normal kidney tissue, and IL1RAP expression was positively correlated with local invasiveness using previously described metrics (ref. 28; Fig. 2E). *IL1RAP* inactivation led to a marked reduction of lung macrometastases and alleviated the overall metastasis burden in mice (Fig. 2F). Notably, although shRNA knockdown effectively reduced IL1RAP expression in primary tumors (Supplementary Fig. S2K), residual lung metastases observed in the *IL1RAP* knockdown groups unexpectedly showed reexpression of IL1RAP comparable to levels in control tumors (Supplementary Fig. S2L), indicating that metastatic cells had either escaped or reversed shRNA-mediated *IL1RAP* depletion. Together, these data highlight an important role for IL1RAP in driving Ewing sarcoma progression, specifically by mediating local invasion and metastatic capacity.

IL1RAP Controls Redox Homeostasis and GSH Pools That Are Vital for Anoikis Resistance in Ewing Sarcoma

The ability to mitigate oxidative stress is strongly linked with the metastatic potential of cancer cells (29–31). Accordingly, we observed that primary tumors with *IL1RAP* depletion were characterized by increased levels of oxidative stress, as evidenced by increased 4-hydroxynonenal (4-HNE) staining (Fig. 2G) and decreased GSH/GSSG ratios (Fig. 2H). In further support of a role for IL1RAP in redox regulation, *IL1RAP* depletion induced ROS accumulation *in vitro* in both 2-D and 3-D cultures (Supplementary Fig. S3A and S3B), which was accompanied by decreased GSH levels (Supplementary Fig. S3C). Strikingly, compared with 2-D growth, ROS levels surged by multiple folds in 3-D cultures, and *IL1RAP* depletion further heightened oxidative stress under these conditions (Supplementary Fig. S3A and S3B), thus offering a potential explanation for the enhanced lethality induced by IL1RAP inactivation in 3-D versus 2-D cultures. As a second ROS challenge, *IL1RAP* knockdown also increased H_2O_2-induced ROS accumulation and sensitized Ewing sarcoma cells to H_2O_2 toxicity (Supplementary Fig. S3D). Further implicating a causal role for oxidative stress in anoikis of Ewing sarcoma cells after *IL1RAP* depletion, anoikis was completely reversed by N-acetylcysteine (NAC) or Trolox antioxidants, or cell-permeable GSH (GSH monoethyl ester or GSH-MEE), in 3-D conditions (Supplementary Fig. S3E and S3F).

To validate that GSH is vital for anoikis resistance in Ewing sarcoma cells, we used buthionine sulfoximine (BSO), an inhibitor of glutamate cysteine ligase (GCL; ref. 32), to induce GSH depletion (Supplementary Fig. S3G). Although severe GSH depletion (e.g., >80% depletion by 8 μmol/L BSO) was required to induce Ewing sarcoma cell death in 2-D cultures (Supplementary Fig. S3H), even mild GSH depletion (e.g., 35% by 1 μmol/L BSO) was lethal to cells in 3-D cultures (Supplementary Fig. S3I). Similar to *IL1RAP* inactivation, BSO-mediated GSH depletion further heightened oxidative stress incurred upon cell detachment (Supplementary Fig. S3J), potentially explaining the higher BSO sensitivity in detached cells. We found that BSO-induced cell death was rescued by antioxidants NAC, Trolox, or GSH-MEE under both 2-D and 3-D cultures (Supplementary Fig. S3K and S3L). This is in contrast to the reported ineffectiveness of BSO in various epithelial tumor types (33) and highlights GSH as a vital regulator of redox homeostasis and, in particular, anoikis resistance in Ewing sarcoma cells. Thus, we have identified IL1RAP as a previously unrecognized mediator of redox homeostasis and anoikis resistance in Ewing sarcoma.

IL1RAP Forms a Complex with CD98 and xCT of the System X_c^- Cystine Transporter

We next determined how IL1RAP is involved in redox homeostasis. In myeloid and leukemia cells, IL1RAP binds to and functions as a cofactor for optimal IL1-mediated binding and IL1R signaling (21, 25). However, in Ewing sarcoma cells, *IL1RAP* depletion failed to attenuate IL1β responsiveness (Supplementary Fig. S4A), whereas IL1RAP-low/negative tumor cells including MCF7 and ZR-75-1 were readily responsive to IL1β stimulation (Supplementary Fig. S4B). These results suggest an IL1-independent role of IL1RAP in Ewing sarcoma. To gain further insights into how IL1RAP functions in Ewing sarcoma, we surveyed the IL1RAP protein interactome by mass spectrometric analysis of immunoprecipitated IL1RAP complexes after formaldehyde cross-linking (Fig. 3A; Supplementary Fig. S4C; Supplementary Table S1). Notably, IL1R1, IL1R2, IL1RL1, or IL1RL2, known IL1RAP interactors in myeloid cells (21), were not detected in our interactome analysis (Supplementary Table S1), and mRNA levels of each are extremely low or absent in Ewing sarcoma (Supplementary Fig. S4D). Among the 21 proteins with fold changes >1.5 and with ≥2 unique peptides identified, along with additional parameters (see Methods), six high-quality candidates emerged as potential IL1RAP interactors (highlighted in red; Supplementary Fig. S4E). Of these, SLC3A2, also known as CD98 (Fig. 3A), was of particular interest, given that it is the heavy chain of the cell-surface system X_c^- cystine transporter that promotes cystine uptake, a rate-limiting substrate for GSH synthesis and redox control (10, 11). We validated the IL1RAP–CD98 interaction using reciprocal co-IPs (Fig. 3B) and IF in A673 Ewing sarcoma cells (Fig. 3C) and in Ewing sarcoma xenografts (Supplementary Fig. S4F). Proximity ligation assays (PLA) independently confirmed IL1RAP–CD98 colocalization both *in vitro* (Fig. 3D) and *in vivo* (Fig. 3E). Similar to the mode of interaction between CD98 and its known light chain partners (17), we found that $CD98^{C109}$ mediates its interaction with IL1RAP via a disulfide bond. First, the reducing agent dithiothreitol (DTT) diminished the IL1RAP–CD98 interaction (Fig. 3B). Second, both reciprocal co-IPs and PLA analysis with HA-tagged CD98 mutants demonstrated that a $CD98^{C109S}$ mutation almost completely abolished the CD98/IL1RAP interaction, in contrast to a control $CD98^{C330S}$ mutation (Fig. 3F; Supplementary Fig. S4G). Third, the Phosphosite database (https://www.phosphosite.org/) predicts that $IL1RAP^{C362}$ (the sixth IL1RAP extracellular residue) is in closest proximity to $CD98^{C109}$ (the fifth CD98 extracellular residue) as a likely mediator of the disulfide bond with $CD98^{C109}$. Indeed, an $IL1RAP^{C362S}$ mutation substantially reduced its

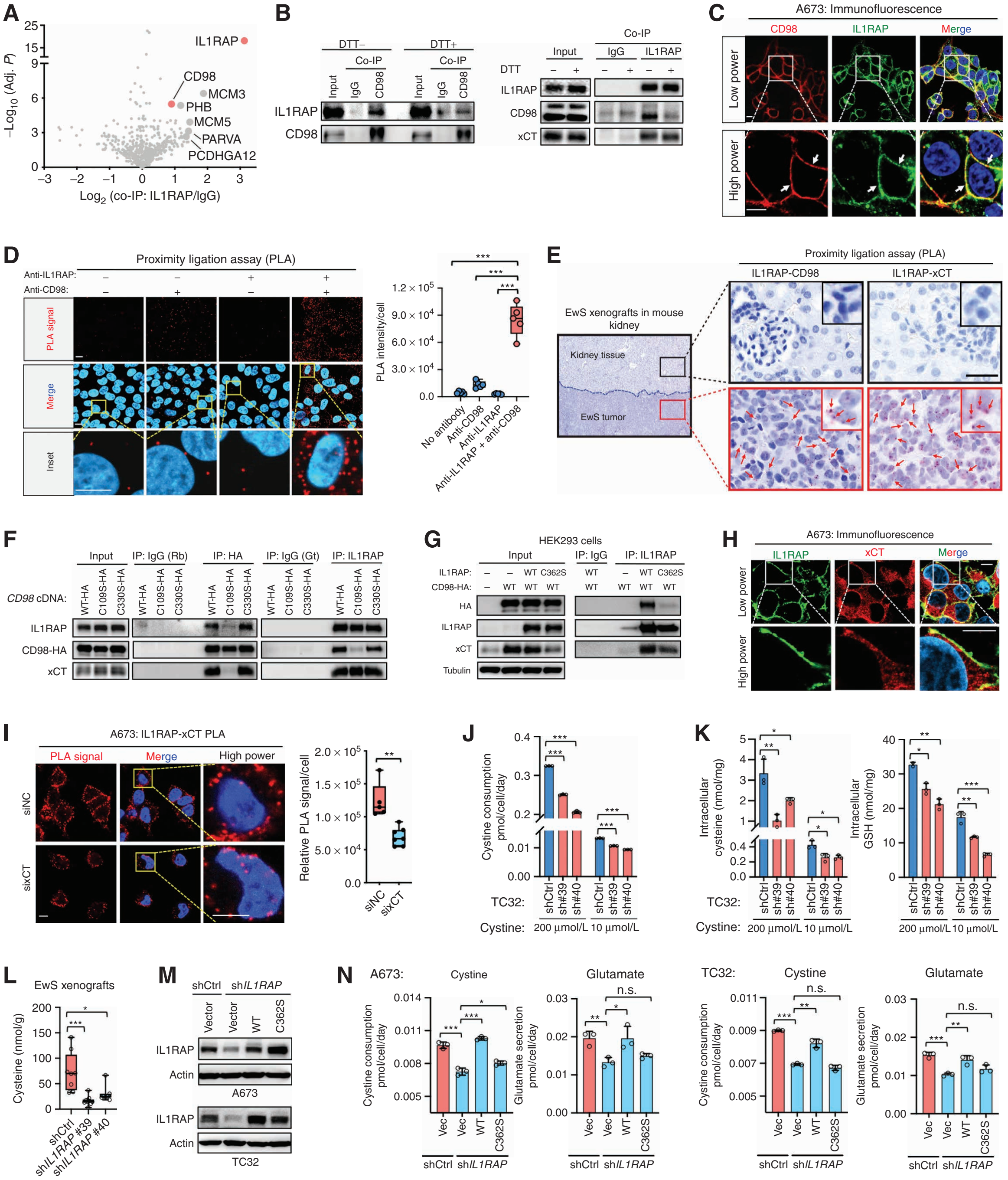

Figure 3. IL1RAP forms a complex with CD98 and xCT of the system X_c^- cystine transporter and promotes cystine uptake. **A,** Volcano plots of proteins identified in the IL1RAP interactome in A673. **B,** Representative immunoblots of the indicated co-IP samples in A673 cells. The experiments were repeated twice with similar results. **C,** Representative IF staining of IL1RAP and CD98 in A673 cells. **D,** PLA of IL1RAP and CD98 in A673 cells ($n = 5$; >100 cells were analyzed for each condition). **E,** PLA of IL1RAP–CD98 or IL1RAP–xCT in TC32-derived Ewing sarcoma (EwS) xenografts in the murine renal subcapsular implantation model. Scale bar, 30 µm; red arrows indicate positive PLA signals in Ewing sarcoma tumor cells. **F,** Representative immunoblots of the indicated co-IP samples in A673 cells expressing wild-type (WT) or mutant CD98 (C109S or C330S). Rabbit (Rb) IgG and goat (Gt) IgG were used as isotype controls for the co-IP experiments. The experiments were repeated twice with similar results. **G,** Representative immunoblots of the indicated co-IP samples in HEK293 cells transfected with WT or mutant IL1RAP (C362S) and WT HA-tagged CD98. **H** and **I,** Representative images showing the IF staining of IL1RAP and xCT (**H**) and PLA assay of IL1RAP and xCT (**I**) in A673 cells. Scale bars, 10 µm. For **I**, $n = 5–7$; ≥50 cells were analyzed for each condition. **J,** The impact of *IL1RAP* knockdown (by sh#39 or #40) on cystine uptake was measured by cystine consumption assay in media containing regular (200 µmol/L) or low (10 µmol/L) levels of cystine. **K** and **L,** Intracellular cysteine and GSH pools were measured in the indicated cell lines (**K**) or Ewing sarcoma xenografts derived from TC32 (**L**) with or without *IL1RAP* knockdown (by sh#39 or #40). **M,** Rescue of WT or mutant IL1RAP (C362S) in Ewing sarcoma cells with *IL1RAP* depletion was determined by immunoblot analysis. **N,** Cystine uptake and glutamate secretion were determined in the indicated Ewing sarcoma cells cultured in media containing 10 µmol/L cystine. Data presented are means ± SD. *, $P < 0.05$; **, $P < 0.01$; ***, $P < 0.001$; P values were determined by two-tailed unpaired Student t test.

interaction with CD98 in HEK293 cells (Fig. 3G). These findings define a novel IL1RAP–CD98 interaction mediated via a disulfide bond between $CD98^{C109}$ and $IL1RAP^{C362}$.

We then probed whether IL1RAP also interacts with xCT, which, together with CD98, forms the system X_c^- cystine transporter (11). An interaction between IL1RAP and xCT was readily detectable in Ewing sarcoma cells by co-IP studies (Fig. 3B and F), IF (Fig. 3H), and PLA analyses (Fig. 3E and I). The IL1RAP–xCT interaction is likely independent of CD98, as DTT, which disrupts the CD98–xCT complex, failed to diminish the observed IL1RAP–xCT association (Fig. 3B, right). Moreover, *CD98* depletion did not reduce IL1RAP–xCT interactions (Supplementary Fig. S4H). Notably, $CD98^{C109}$, forming a disulfide bond with $IL1RAP^{C362}$, is also known to be critical for CD98–xCT interactions in other cell types (17, 34), which we validated in Ewing sarcoma cells (Fig. 3F). These results suggest that CD98 can form disulfide bridges with both IL1RAP and xCT via the same $CD98^{C109}$ residue. Because this residue would not be expected to bind both IL1RAP and xCT simultaneously, our data point to the possibility that IL1RAP or xCT separately interacts covalently with CD98, and these heterodimers further interact to form larger complexes involving all three proteins.

CD98 is known to be required for xCT surface localization and protein stability (34). Indeed, overall and plasma membrane–localized xCT levels were reduced by *CD98* depletion in Ewing sarcoma cells, but neither IL1RAP surface localization nor its expression was affected by *CD98* knockdown (Supplementary Fig. S4I). Given that IL1RAP interacts with both CD98 and xCT, we tested if IL1RAP is required for the CD98–xCT interaction. However, *IL1RAP* depletion failed to disrupt the CD98–xCT complex (Supplementary Fig. S4J), and in contrast to *CD98* knockdown, *IL1RAP* depletion did not reduce xCT expression levels (Supplementary Fig. S4K). Similarly, *IL1RAP* knockdown did not affect binding to other known CD98 interactors, LAT1 and LAT2 (Supplementary Fig. S4L). Together, these findings characterize IL1RAP as a new partner of the system X_c^- cystine transporter that interacts with both CD98 and xCT, although the overall stoichiometry remains to be determined.

IL1RAP Augments System X_c^- Activity to Maintain Intracellular Cysteine and GSH Pools

Given that IL1RAP forms a complex with CD98 and xCT in Ewing sarcoma cells, we hypothesized that it may boost cystine uptake by facilitating system X_c^- activity to maintain cysteine pools and redox homeostasis. To test this, we first confirmed that extracellular cystine is critical for redox control and cell survival in Ewing sarcoma cells *in vitro*. Indeed, reducing extracellular cystine levels triggered ROS accumulation and cell death of Ewing sarcoma cell lines (Supplementary Fig. S5A), both of which were markedly potentiated by *IL1RAP* depletion (Supplementary Fig. S5A). This suggests an important role of IL1RAP in maintaining redox homeostasis associated with cystine supply, particularly under cystine-depleted conditions. We next performed cystine consumption assays to evaluate if IL1RAP modulates cystine uptake, under both cystine-replete (200 μmol/L) and cystine-depleted (10 μmol/L) conditions. We found that *IL1RAP* depletion significantly impaired cystine uptake, as measured by cystine consumption assays, under both conditions (Fig. 3J). In keeping with this, intracellular cysteine and GSH pools were each significantly reduced in cells with *IL1RAP* depletion compared with controls, and levels were further reduced at 10 μmol/L versus 200 μmol/L extracellular cystine concentrations (Fig. 3K). These data were corroborated by our *in vivo* studies, revealing markedly decreased cysteine pools in Ewing sarcoma xenografts with *IL1RAP* depletion compared with controls (Fig. 3L), mirroring their high oxidative stress (Fig. 2G and H).

To further probe effects of IL1RAP on xCT activity, we next determined if IL1RAP regulates glutamate secretion, as the xCT antiporter mediates glutamate secretion in exchange for cystine uptake (17). In control experiments, glutamate secretion was higher in the presence of 200 μmol/L extracellular cystine compared with 10 μmol/L cystine, and secretion was strongly inhibited by erastin (Supplementary Fig. S5B), a potent xCT inhibitor (14). *IL1RAP* depletion reduced glutamate secretion under both high (200 μmol/L) and low (10 μmol/L) extracellular cystine conditions in both TC32 and A673 Ewing sarcoma cell lines (Supplementary Fig. S5B), mirroring results of the cystine consumption assays. We found that the IL1RAP and CD98 interaction is critical for enhanced system X_c^- activity, as expression of an shRNA-resistant $IL1RAP^{C362S}$ mutant that cannot interact with CD98 (Fig. 3M) was ineffective in rescuing cystine uptake or glutamate secretion in IL1RAP-depleted cells, whereas wild-type (WT) IL1RAP could almost fully rescue these phenotypes (Fig. 3N).

Finally, confirming that cysteine replenishment by IL1RAP is critical for maintaining GSH levels and redox homeostasis, we found that *IL1RAP* depletion further reduced GSH levels already suppressed by xCT blockade by erastin or sulfasalazine (SAS; ref. 35) or xCT knockdown (Supplementary Fig. S5C). Accordingly, pharmacologic xCT blockade increased ROS levels and synergized with *IL1RAP* depletion to exacerbate ROS accumulation (Supplementary Fig. S5D).

Blocking IL1RAP Enhances Ferroptosis

To further explore the biological function of IL1RAP in regulating system X_c^-, we investigated its role in ferroptosis, i.e., iron-dependent cell death triggered by cysteine deficiency (14, 36). Similar to other tumor types (15), blocking system X_c^- in Ewing sarcoma cells by either erastin treatment or *CD98* knockdown led to diminished GSH pools (Supplementary Fig. S5E), increased lipid ROS levels (Supplementary Fig. S5F), and triggered ferroptosis that was fully rescued by ferrostatin-1 (Fer-1), a potent inhibitor of ferroptosis (ref. 14; Supplementary Fig. S5G). Although *IL1RAP* depletion alone only slightly affected lipid ROS and ferroptosis under ambient conditions, it markedly potentiated lipid oxidation (Supplementary Fig. S5H) and ferroptosis (Supplementary Fig. S5I) in the presence of erastin, which were each fully reversed by Fer-1. NAC and Trolox also reversed GSH depletion induced by *IL1RAP* knockdown or erastin treatment in Ewing sarcoma cells (Supplementary Fig. S5J) and effectively rescued these cells from ferroptosis (Supplementary Fig. S5K), validating the importance of GSH antioxidants in this phenotype. Furthermore, we found a link between anoikis and ferroptosis, as growth of Ewing sarcoma cells in 3-D cultures led to enhanced lipid ROS compared with 2-D cultures, and *IL1RAP* depletion further exacerbated this effect

(Supplementary Fig. S5L). Accordingly, soft-agar colony formation blocked by *IL1RAP* depletion was at least partially rescued by Fer-1 (Supplementary Fig. S5M). Taken together, these results demonstrate that IL1RAP boosts system X_c^- activity in Ewing sarcoma cells to maintain cysteine and GSH pools for redox homeostasis and protection from ferroptosis.

IL1RAP Controls the Transsulfuration Pathway to Replenish Cysteine and GSH Pools When Cystine Uptake Is Limited

In addition to conversion from cystine, synthesis of cysteine can also occur *de novo* via the TSS pathway (Fig. 4A) when extracellular cystine supply or uptake is limited (11, 18). Indeed, erastin-treated Ewing sarcoma cells initiated potent feedback activation of TSS by sharply increasing *CTH* and *CBS* mRNAs (Supplementary Fig. S6A), which encode two key TSS enzymes (11). We therefore expected that *IL1RAP* depletion, by reducing cystine uptake via xCT inhibition, would lead to activation of the TSS pathway. Surprisingly, however, when cystine uptake was blocked by either erastin or *xCT* knockdown, *IL1RAP* depletion further reduced GSH and increased ROS levels (Supplementary Fig. S5D and S5E). We therefore wondered if IL1RAP also promotes *de novo* cysteine replenishment via the TSS pathway in Ewing sarcoma cells. To explore this in an unbiased manner, we performed proteomics to determine changes in global protein expression in 3-D-cultured Ewing sarcoma cells following *IL1RAP* depletion by two independent shRNAs (schema in Fig. 4B), allowing us to catalog alterations common to both shRNAs ($r = 0.54$, $P < 0.0001$; Fig. 4C; Supplementary Table S2). Strikingly, CTH was among the top downregulated hits following *IL1RAP* knockdown (Fig. 4C), suggesting that CTH induction occurs downstream of IL1RAP. Accordingly, *IL1RAP* knockdown reduced CTH at both the mRNA and protein levels *in vitro* (Supplementary Fig. S6B and S6C), and, importantly, erastin-induced compensational activation of CTH expression was blocked by *IL1RAP* depletion (Fig. 4D). A functional IL1RAP–CTH axis was also confirmed *in vivo*, as *IL1RAP* depletion reduced CTH expression in Ewing sarcoma xenografts (Supplementary Fig. S6D). Moreover, *CTH* expression was positively correlated with *IL1RAP* expression in a panel of Ewing sarcoma cells (Supplementary Fig. S6E). In keeping with reduced *CTH* mRNA transcripts upon *IL1RAP* depletion (Supplementary Fig. S6C), we observed a proportional reduction of *CTH* polysome-bound (i.e., translationally active) transcripts in sucrose gradient fractionated RNA (Supplementary Fig. S6F). These data argue that CTH expression is transcriptionally rather than translationally regulated downstream of IL1RAP. Moreover, we did not observe significant changes in global mRNA translation upon *IL1RAP* depletion (Supplementary Fig. S6G). Clinically, and supporting a role for CTH in Ewing sarcoma pathobiology, high *CTH* expression is associated with shorter event-free survival in two separate cohorts of patients with Ewing sarcoma (Supplementary Fig. S6H). Together, these data suggest that Ewing sarcoma cells can utilize a putative IL1RAP–CTH axis to replenish cysteine and GSH supply when cystine uptake is limited.

We confirmed that CTH is crucial for Ewing sarcoma cell survival under partial cystine deprivation, as *CTH* knockdown markedly increased cell death in both A673 cells (Fig. 4E) and TC32 cells (Supplementary Fig. S6I) under low cystine conditions (cystine 10 μmol/L). However, complete cystine depletion induced massive cell death and growth inhibition of both control and *CTH* knockdown cells (Fig. 4E; Supplementary Fig. S6I). This indicates that *de novo* cysteine synthesis alone is insufficient to support Ewing sarcoma cell survival, and a basal level of extracellular cystine supply is required. We wondered if this is due to a limited availability of substrates for TSS in the absence of cystine, as reported recently in other systems (18). In support of this, supplementing homocysteine (Hcy), a key substrate for TSS (Fig. 4A), in cystine-free media strongly rescued cell survival and growth in control Ewing sarcoma cells, whereas this effect was almost completely abolished by *CTH* depletion (Fig. 4E; Supplementary Fig. S6I). Accordingly, Hcy supplementation (for 12 hours) in control cells increased the TSS metabolite cystathionine and cysteine-containing γ-glutamyl-cysteine and GSH, whereas *CTH* knockdown led to a buildup of Hcy and cystathionine and decreased γ-glutamyl-cysteine and GSH levels (Fig. 4F; Supplementary Fig. S6J). Of note, despite the strong rescue of γ-glutamyl-cysteine and GSH (which both contain cysteine) by Hcy under cystine starvation, we did not observe rescue of cysteine itself under this condition (Fig. 4F; Supplementary Fig. S6J), in line with the very recent finding that high ROS (such as is induced by cystine depletion) rapidly sequesters cysteine for GSH synthesis (37). Our data again support a causal role for GSH and redox homeostasis in CTH-mediated cell survival, as supplementation with GSH-MEE or other antioxidants strongly rescued cell survival under cystine deprivation in *CTH* knockdown cells (Supplementary Fig. S7A). In contrast, Na2S, GYY4137, or AP39, donors of H2S, a gaseous metabolite promoted by CTH from the TSS pathway (38), were ineffective in rescuing survival in *CTH* knockdown cells under the same conditions (Supplementary Fig. S7A).

Finally, to directly test if a putative IL1RAP–CTH axis contributes to cysteine and GSH replenishment when cystine is limited, we performed metabolic flux analysis of ^{13}C-serine, a key precursor for cysteine synthesis via the TSS pathway (Fig. 4A). Since we (Fig. 4F; Supplementary Fig. S6J) and others (37) have shown that cysteine is metabolized to γ-glutamyl-cysteine and GSH during cystine deprivation, we used a protocol recently published by the Thompson laboratory to effectively trace newly synthesized cysteine production (18), i.e., supplementing the media with 2-mercaptoethanol to maintain redox homeostasis upon cystine depletion. In support of a functional IL1RAP–CTH axis, *IL1RAP* knockdown markedly diminished ^{13}C-serine to ^{13}C-cysteine conversion and downstream ^{13}C-GSH pools, each of which could be strongly rescued by CTH reexpression (Fig. 4G). This mechanism also protected Ewing sarcoma cells from ferroptosis during cystine starvation; *CTH* depletion markedly exacerbated lipid ROS accumulation, which was almost fully reversed by Fer-1 (Supplementary Fig. S7B). Accordingly, *CTH* depletion rendered Ewing sarcoma cells highly susceptible to ferroptosis induced by erastin, which was rescued by Fer-1, NAC, or Trolox (Supplementary Fig. S7C). Reexpression of CTH in *CTH* knockdown cells mitigated lipid ROS accumulation and rescued cell survival (Supplementary Fig. S7D and S7E), pointing to a causal role for CTH in these processes. *CTH* reexpression also rescued *IL1RAP*-depleted cells from severe GSH depletion (Fig. 4H), as well as lipid

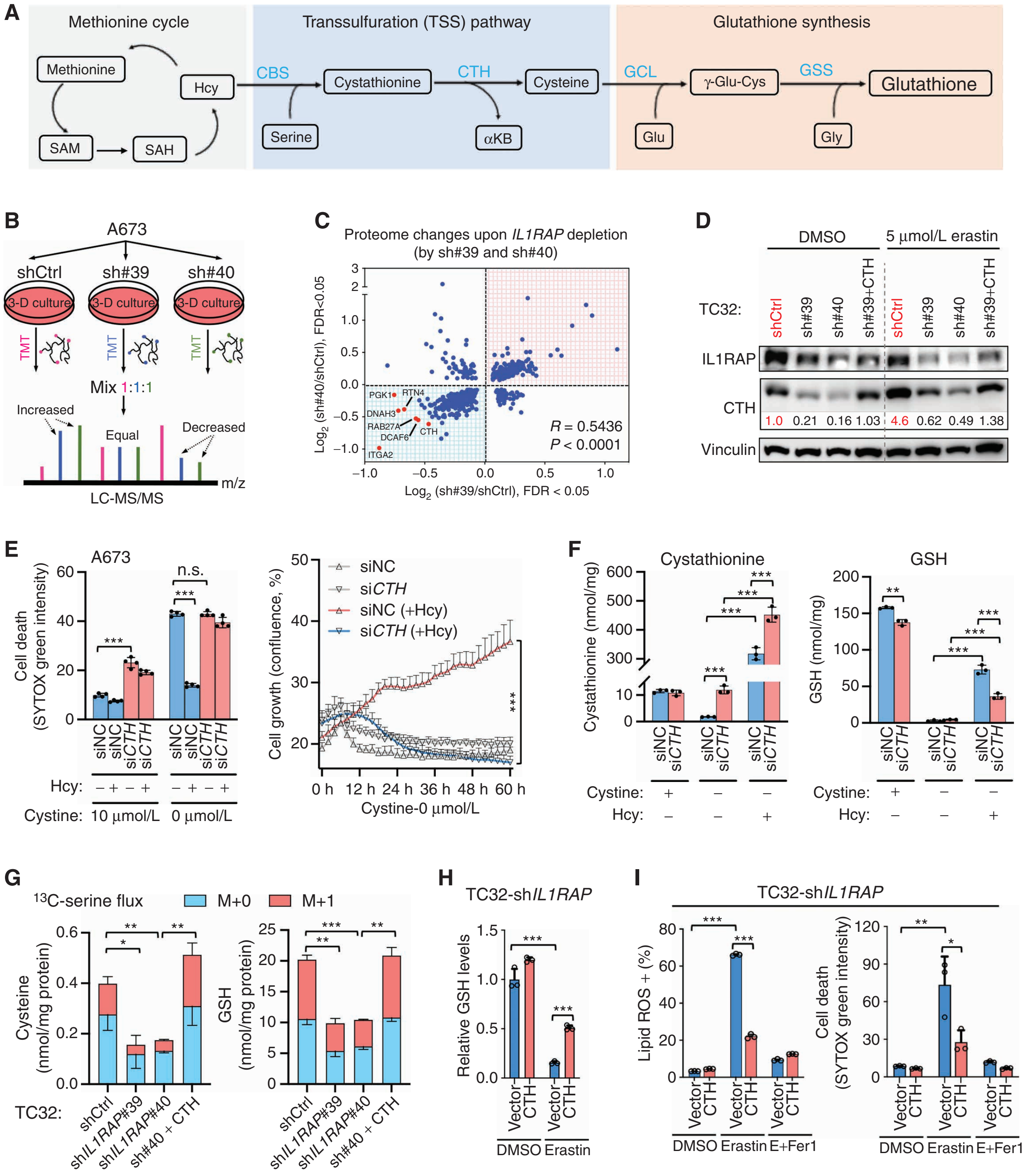

Figure 4. The IL1RAP–CTH axis promotes the TSS pathway. **A,** Schematic showing the pathway that mediates *de novo* cysteine synthesis and GSH production via TSS. **B,** Schematic showing the global proteome analysis in A673 Ewing sarcoma cells with control knockdown (shCtrl) or *IL1RAP* knockdown (sh#39 and sh#40) grown in 3-D cultures. **C,** Global proteome changes induced by *IL1RAP* depletion with two independent shRNAs ($n = 3$ biologically independent samples). **D,** Immunoblot analysis of the indicated proteins. Densitometry analysis of CTH normalized to the vinculin loading control is shown. The experiment was repeated twice with similar results. **E,** Cell death and cell growth were measured by Incucyte in the indicated cells cultured in media containing different concentrations of cystine supplemented with/without 0.4 mmol/L homocysteine (Hcy). **F,** Intracellular levels of cystathionine and GSH were determined in cells cultured in media ± 200 µmol/L cystine or 0.4 mmol/L Hcy for 12 hours. **G,** *De novo* cysteine synthesis and GSH production in the indicated cells were determined in cystine-depleted cultures by flux analysis of ^{13}C-serine, a key substrate for the TSS pathway as shown in **A**. ^{12}C-labeled (M + 0) and 13C-labeled (M+1) metabolites were measured after 24 hours. **H** and **I,** The effects of CTH reexpression on GSH pools (12 hours; **H**), lipid ROS accumulation (22 hours; **I**, left), and cell death (48 hours; **I**, right) in *IL1RAP*-depleted cells with the indicated treatments. 2 and 5 µmol/L erastin was used in **H** and **I**, respectively; and 2 µmol/L Fer-1 was used in **I**. *P* values were determined by two-tailed unpaired Student *t* test; *, $P < 0.05$; **, $P < 0.01$; ***, $P < 0.001$.

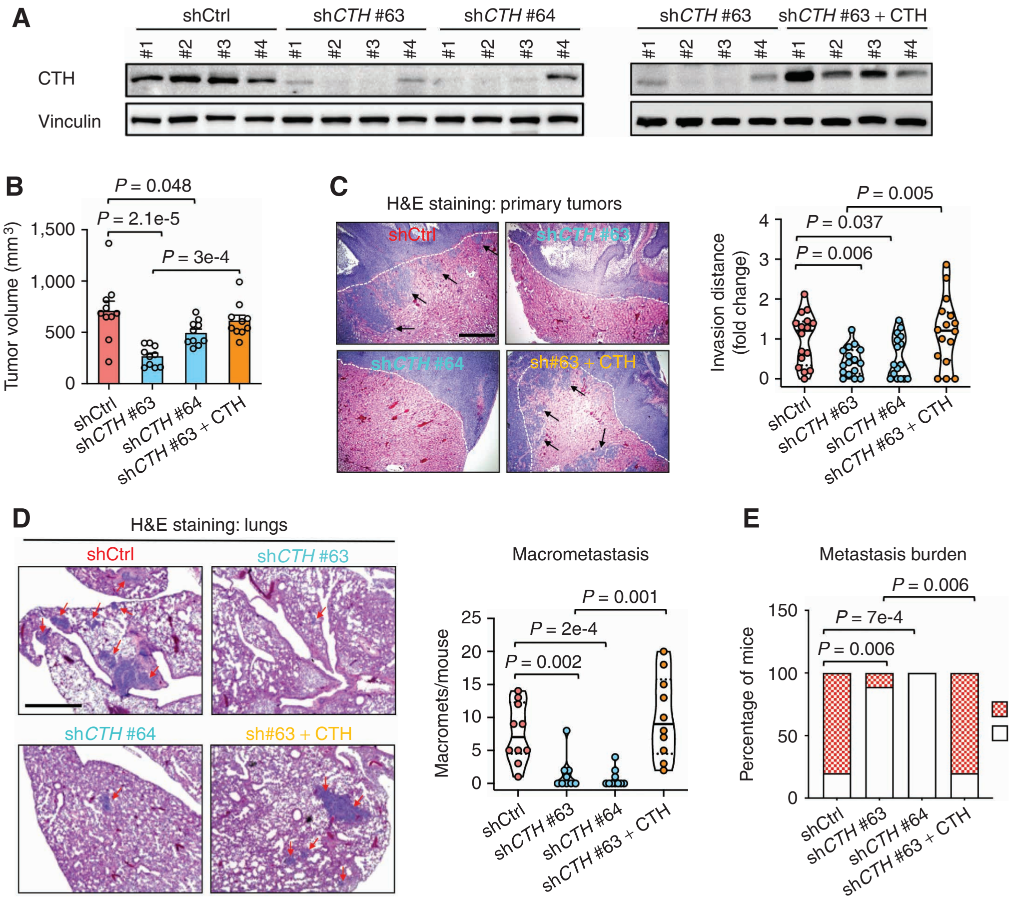

Figure 5. CTH promotes invasion and metastasis in Ewing sarcoma. **A,** Immunoblot analysis in lysates of TC32-derived Ewing sarcoma xenograft tumors in mice ($n = 4$ independent tumors). **B,** Volumes of TC32-derived Ewing sarcoma tumors in the renal subcapsular space of mice ($n = 10$). **C,** H&E staining of TC32-derived tumors in the renal subcapsular space of mice and quantification of local invasion distance ($n = 10$). Dashed lines indicate the boundaries between primary Ewing sarcoma tumors and the surrounding kidney tissues; arrows indicate invasive Ewing sarcoma cells. Scale bar, 50 μm. **D,** Left, H&E staining of lung sections from mice implanted with Ewing sarcoma (TC32) tumors in the renal subcapsular space. Arrows indicate Ewing sarcoma metastases. Scale bar, 300 μm. Right, quantifications of macrometastases in the lungs ($n = 10$). **E,** The metastatic burden in the lungs of each group (see Methods for details). In **B**, data, means ± SEM. In **C** and **D**, the lines in the violin plots show the median and interquartile range. *P* values were determined by two-tailed unpaired Student *t* test.

ROS accumulation and ferroptosis (Fig. 4I), further supporting CTH as a direct functional mediator of IL1RAP in ferroptosis resistance under cystine deficiency. Although the exact mechanism by which IL1RAP upregulates CTH expression is unknown and may be indirect, our findings demonstrate that in addition to regulating xCT-mediated cystine uptake, IL1RAP is also deployed by Ewing sarcoma cells to control CTH expression and the TSS pathway to replenish cysteine and GSH when cystine is limited.

CTH Promotes Invasion and Metastasis in Ewing Sarcoma

We next assessed if, similar to IL1RAP, CTH influences Ewing sarcoma primary tumor growth and metastasis *in vivo*. Using the above murine renal subcapsular implantation model, *CTH* depletion reduced primary tumor growth by 30% to 60%, which was restored by reexpression of a non-shRNA targeted *CTH* construct (Fig. 5A and B). Analysis of invasive margins of the implanted Ewing sarcoma tumors revealed that *CTH* depletion markedly decreased local invasion into neighboring kidney tissues (Fig. 5C), which was fully rescued by *CTH* reexpression. Strikingly, *CTH* depletion substantially reduced lung macrometastases by 5–10-fold (Fig. 5D) and alleviated the metastasis burden in mice (Fig. 5E), which could be fully rescued by *CTH* reexpression. Moreover, *CTH* depletion prolonged tumor-free survival in mice (Supplementary Fig. S8A), supporting the importance of CTH expression in Ewing sarcoma oncogenesis. Similar to *IL1RAP* depletion, *CTH* knockdown significantly decreased intracellular cysteine pools (Supplementary Fig. S8B) and increased oxidative stress *in vivo*, as evidenced by significantly enhanced 4-HNE staining (Supplementary Fig. S8C), and both could be rescued by *CTH* reexpression. These findings demonstrate that CTH, as a downstream effector of IL1RAP, is a critical prometastatic factor in Ewing sarcoma.

EWS–FLI1 Directly Regulates *IL1RAP* Expression via Enhancer Activation

Given our initial finding that mutant KRAS and ETV6–NTRK3 induce IL1RAP in 3-D cultures, we wondered if Ewing

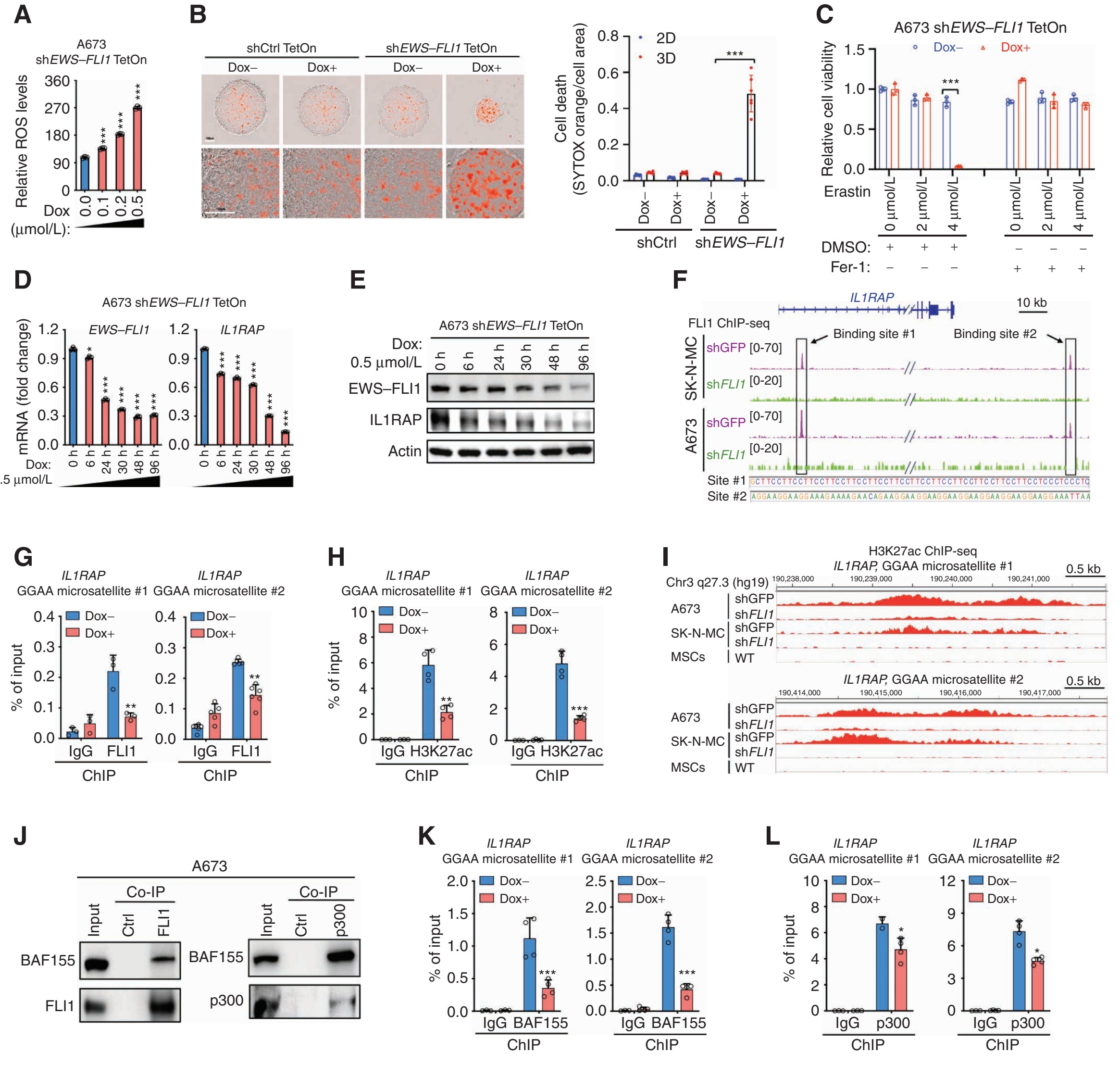

Figure 6. EWS–FLI1 directly regulates *IL1RAP* expression via enhancer activation. **A,** Flow cytometry–based quantification of ROS (CellROX Deep Red) 96 hours after Dox treatment. **B,** Incucyte analysis of SYTOX orange staining (red) in 2-D and 3-D cultures to evaluate cell death. The ratio between SYTOX orange intensity and cell area was calculated ($n = 6$). Scale bar, 100 μm. **C,** Relative cell viability in the indicated cells was measured by CCK-8 assay after 24-hour treatment ($n = 3$). **D,** *EWS–FLI1* and *IL1RAP* mRNA expression in the indicated samples determined by qPCR ($n = 3$). **E,** Immunoblotting analysis of the indicated proteins. The experiment was repeated over three times with similar results. **F,** ChIP-seq results of FLI1 in the indicated cells with shGFP control knockdown or sh*FLI1* knockdown (48 hours; GEO: GSE61953). **G** and **H,** ChIP-qPCR assays were performed to determine the occupancy of EWS–FLI1 and H3K27ac at the *IL1RAP* locus in A673 Ewing sarcoma cells with Dox-inducible knockdown of *EWS–FLI1* (0.5 μmol/L Dox, 72 hours). **I,** ChIP-seq results of H3K27ac in the indicated cells with shGFP control knockdown or sh*FLI1* knockdown (48 hours; GEO: GSE61953). **J,** Representative immunoblots of the indicated samples. The experiment was repeated twice with similar results. **K** and **L,** ChIP-qPCR assays were performed to determine the occupancy of BAF155 and p300 at the *IL1RAP* locus in A673 Ewing sarcoma cells with Dox-inducible knockdown of *EWS–FLI1* (0.5 μmol/L Dox, 72 hours). For all panels, data, means ± SD. *, $P < 0.05$; **, $P < 0.01$; ***, $P < 0.001$; P values were determined by two-tailed unpaired Student t test.

sarcoma fusion oncoproteins, namely, EWS–FLI1 (85%–90% of cases) and EWS–ERG (~10%–15% of cases; ref. 3), might also activate IL1RAP expression. To test this, we modeled *EWS–FLI1* inactivation using a doxycycline (Dox)-inducible shRNA knockdown system in A673 cells, as described (39). *EWS–FLI1* depletion markedly induced ROS accumulation in a dose-dependent fashion (Fig. 6A) compared with Dox-alone controls (Supplementary Fig. S9A). *EWS–FLI1* depletion also rapidly triggered anoikis in 3-D cultures and completely blocked colony formation in soft agar (Fig. 6B; Supplementary Fig. S9B and S9C), whereas only mild cytostatic effects were observed in 2-D cultures (Supplementary Fig. S9D). Moreover, upon cystine uptake blockade by erastin, cells with *EWS–FLI1* depletion underwent massive ferroptosis that could be fully rescued by Fer-1 (Fig. 6C). These results indicate that EWS–FLI1 regulates ROS detoxification and confers resistance to both anoikis and ferroptosis.

Because EWS–FLI1 is a chimeric transcription factor, we tested if it directly regulates the expression of *IL1RAP*. *EWS–FLI1* depletion reduced IL1RAP expression at both mRNA and protein levels in a time-dependent manner (Fig. 6D and E), and transient ectopic expression of EWS–FLI1 or EWS–ERG in HEK293 cells induced IL1RAP expression (Supplementary

Fig. S9E). Moreover, we observed significant correlations between *EWS–FLI1* and *IL1RAP* mRNA expression across independent Ewing sarcoma patient cohorts (Supplementary Fig. S9F). CTH, a downstream effector of IL1RAP, is also regulated by Ewing sarcoma fusion oncoproteins, as evidenced by its induction when Ewing sarcoma fusions were overexpressed in HEK293 cells (Supplementary Fig. S9E), or suppression in A673 cells with EWS–FLI1 inactivation (compare vector-alone lanes in Supplementary Fig. S9G and S9H ± Dox treatment). Nonetheless, CTH regulation by EWS–FLI1 is likely indirect and through IL1RAP, as *IL1RAP* reexpression in *EWS–FLI1* knockdown cells rescued *CTH* mRNA and protein expression without affecting *EWS–FLI1* levels (Supplementary Fig. S9G and S9H). These results indicate that Ewing sarcoma fusions regulate the IL1RAP–CTH axis.

EWS–FLI1 appears to directly control *IL1RAP* transcription, as both endogenous and ectopically expressed EWS–FLI1 bind to the *IL1RAP* locus (Fig. 6F; Supplementary Fig. S9I), based on publicly available FLI1 chromatin immunoprecipitation sequencing (ChIP-seq) data from others (39, 40). We identified two binding sites, one within intron 1 and another located ~40 kb downstream of the *IL1RAP* locus, with both sites comprising GGAA microsatellites (Fig. 6F), known consensus binding elements for EWS–FLI1 and EWS–ERG (39–42). Using ChIP-qPCR, we verified that EWS–FLI1 binds to both GGAA microsatellites at the *IL1RAP* locus (Fig. 6G) as well as that of the *SOX2* positive control (Supplementary Fig. S9J). Next, we explored how EWS–FLI1 activates *IL1RAP* transcription. Because the *IL1RAP*-associated GGAA microsatellites are intronic and intergenic, respectively, we reasoned that the transcriptional regulation of *IL1RAP* by EWS–FLI1 is through enhancer activation. Indeed, H3K27ac, an activating histone marker, was enriched at both *IL1RAP* GGAA microsatellites, and *EWS–FLI1* knockdown markedly reduced that modification (Fig. 6H). A similar effect was observed at the positive control *SOX2* locus (Supplementary Fig. S9J). This was fully corroborated by H3K27ac ChIP-seq results from previous studies (refs. 39, 40; Fig. 6I). Control MSCs had almost no detectable H3K27ac at these sites (Fig. 6I), mirroring the low IL1RAP expression observed in MSCs compared with Ewing sarcoma cells (Supplementary Fig. S2D and S2E). In support of the causal role of EWS–FLI1 in the regulation of this histone mark at the *IL1RAP* locus, ectopic expression of *EWS–FLI1* induced H3K27ac at both sites (Supplementary Fig. S9K).

We next investigated how EWS–FLI1 controls enhancer activation of *IL1RAP*. We reasoned that because the canonical BRG1/BRM-associated factor (BAF) complex is a key functional mediator of EWS–FLI1 chromatin binding (40), and histone acetyltransferase p300 facilitates BAF complex–regulated chromatin remodeling (43), EWS–FLI1 likely recruits the BAF/p300 complex to the *IL1RAP* locus for gene activation. In support of this, co-IP analysis confirmed that EWS–FLI1, BAF155 (a core component of the BAF complex), and p300 form a complex in Ewing sarcoma cells (Fig. 6J). Secondly, ChIP-qPCR analysis showed that both BAF155 and p300 bind each of the two GGAA microsatellites within the *IL1RAP* locus (Fig. 6K and L), as well as the positive control *SOX2* locus (Supplementary Fig. S9J), both of which were diminished by *EWS–FLI1* knockdown. This was corroborated by analysis of published ChIP-seq data (39, 40), demonstrating EWS–FLI1-dependent binding of both BAF155 and p300 to the same two *IL1RAP* GGAA microsatellites (Supplementary Fig. S9L). Finally, depletion of *BAF155* or *p300* each significantly reduced *IL1RAP* expression in Ewing sarcoma cells (Supplementary Fig. S9M and S9N), albeit moderately upon *p300* knockdown. Together, these data indicate that EWS–FLI1 stimulates *IL1RAP* enhancer activation by recruiting the BAF155/p300 chromatin remodeling complex to *IL1RAP*-associated GGAA repeats.

IL1RAP Is a Potential Cell-Surface Therapeutic Target in Ewing Sarcoma

Given its association with aggressive disease and cell-surface localization in Ewing sarcoma, we explored if IL1RAP can be used as a target for potential immunotherapy. To determine specificity for cancer cells while leaving healthy tissues intact, we first determined the expression profile of IL1RAP in normal tissues. IHC staining of IL1RAP in tissue microarrays (TMA) revealed that although IL1RAP was highly expressed in Ewing sarcoma tumors, minimal to negative staining was found in all normal pediatric (24 types) or adult (18 types) tissues tested, except for placenta (Fig. 7A; Supplementary Fig. S10A). Moreover, compared with Ewing sarcoma cells, IL1RAP protein expression was substantially lower in both cord blood and healthy adult blood samples (Fig. 7B). To identify potential therapeutic antibodies targeting surface IL1RAP, we panned a human antibody domain (V_H) phage-displayed library against the recombinant ectodomain of IL1RAP as an antigen. We identified a panel of IL1RAP binders (Supplementary Fig. S10B), one of which, V_H X1, was chosen for generation of a fully human V_H–Fc fusion protein (V_H–Fc X1) where Fc is an IgG1 Fc. V_H–Fc X1 is highly specific for IL1RAP, as both IF (Fig. 7C) and flow cytometry (Fig. 7D) analyses showed strong surface binding in Ewing sarcoma cell lines that were IL1RAP-positive, whereas minimal binding was observed in U2OS and MDA-MB-231 cells, two lines expressing very low IL1RAP levels (Fig. 2C; Supplementary Fig. S2C). Moreover, Ewing sarcoma cells were able to effectively internalize the surface bound V_H–Fc X1 (Supplementary Fig. S10C). Notably, V_H–Fc X1 was able to trigger antibody-dependent cellular cytotoxicity (ADCC) in an ADCC reporter cell line in the presence of Ewing sarcoma target cells (Fig. 7E), and in a panel of Ewing sarcoma cell lines when cocultured with peripheral blood mononuclear cells (PBMC; Fig. 7F). Thus, we have identified IL1RAP as a highly expressed surface protein in Ewing sarcoma for potential immunotherapeutic targeting.

DISCUSSION

Despite extensive research into mechanisms underpinning metastasis, effective targets for antimetastasis therapy continue to be elusive, and metastatic disease remains the leading cause of cancer-associated mortality (1, 2), including Ewing sarcoma (3). Given extensive literature that disseminated tumor cells must suppress anoikis before metastatic colonization can occur in distant organs (4), we focused our integrated translatomic and proteomic screens on anti-anoikis factors, and uncovered the IL1RAP cell-surface protein as a previously unknown suppressor of anoikis and a driver of metastasis in Ewing sarcoma.

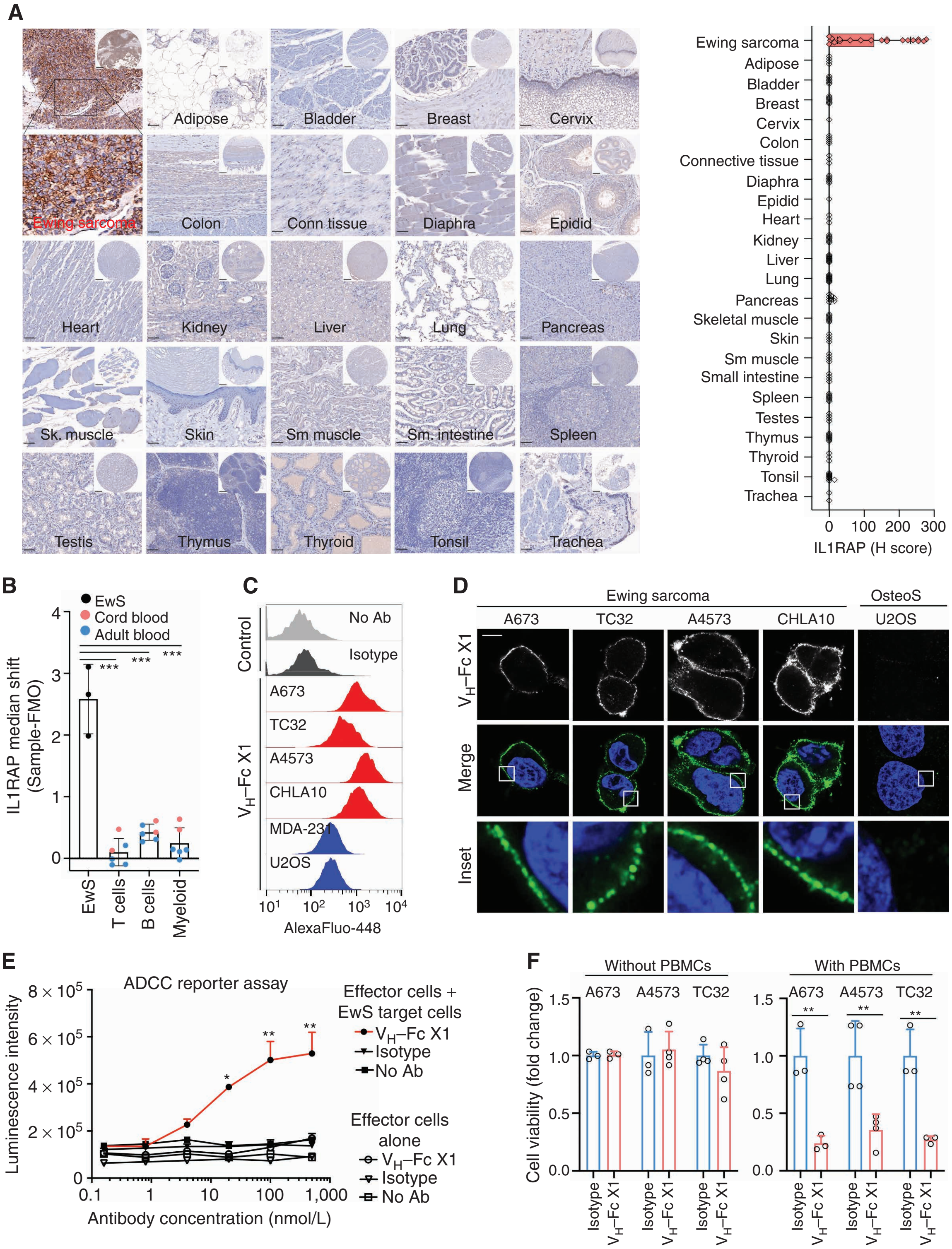

Figure 7. IL1RAP is a potential cell-surface therapeutic target in Ewing sarcoma (EwS). **A,** IHC analysis of IL1RAP in pediatric normal organ TMAs. Scale bars, 50 μm in high-power images and 200 μm in low-power images. **B,** Median asinh (signal/150) differences in IL1RAP intensity of the indicated stained cells from their corresponding FMO (fluorescence minus one) control. **C** and **D,** Binding of the IL1RAP antibody V_H-Fc X1 to a panel of human cancer cell lines was determined by flow cytometry (**C**) and IF analysis (**D**). Scale bar, 10 μm. **E,** The ADCC reporter assay was performed using the Jurkat T-NFAT-Luc-CD16A effector cells encoding the luciferase reporter gene driven by the nuclear factor of activated T cells response element (NFAT-RE). A673 Ewing sarcoma cells were used as target cells. Target:effector cell ratio, 1:6. An isotype control or no antibody was added in the control groups. Baseline reporter activity was determined by omitting the Ewing sarcoma target cells in the assay. **F,** ADCC assays using PBMCs as effector cells and a panel of Ewing sarcoma cells as target cells ($n = 3$–4). Target:effector cell ratio, 1:15. All data presented are means ± SD. In **B**, one-sample *t* test was performed, and two-tailed unpaired Student *t* test was used in other panels. *, $P < 0.05$; **, $P < 0.01$; ***, $P < 0.001$.

As a rate-limiting substrate for GSH synthesis (10, 11, 17), cysteine is a conditionally essential amino acid acquired through extracellular uptake via system Xc^- as well as *de novo* synthesis via the TSS pathway (11, 18). Both the present study and others (11, 18) show that cancer cells can initiate feedback activation of the TSS pathway when the extracellular cystine supply is limited. However, to date, no factor has been described that connects these two closely related but distinct metabolic processes. Unexpectedly, we uncover that in Ewing sarcoma cells, IL1RAP not only augments cystine uptake but also promotes cysteine replenishment under extracellular cystine deficiency. IL1RAP mediates these functions via complexing with the xCT/CD98 cystine transporter to enhance cystine transport, but also promotes expression of CTH, a key enzyme in the TSS pathway. Because extracellular cystine shortage is frequently encountered by tumor cells *in vivo* (44), enhanced intracellular cysteine supply through IL1RAP and the TSS confers resistance to redox stress-induced forms of cell death such as anoikis and ferroptosis, which may contribute to enhanced metastatic capacity in Ewing sarcoma. As such, IL1RAP promotes two related but distinct processes for tumor-associated cysteine and GSH replenishment, highlighting IL1RAP inhibition as a unifying strategy for blocking cysteine metabolism in certain cancer cells expressing this surface protein.

Our data indicate that in Ewing sarcoma cells, IL1RAP and components of the system X_c^- transporter assemble into a novel complex to enhance cystine uptake under both cystine-replete and cystine-depleted conditions. Other surface binding partners of system X_c^-, such as CD44 variant (CD44v), also promote GSH-mediated redox control and tumorigenicity by enhancing cystine uptake in gastric cancers (45). However, unlike CD44v, IL1RAP does not regulate the expression or stability of xCT in Ewing sarcoma. Instead, IL1RAP binds to CD98 via a $CD98^{C109}/IL1RAP^{C362}$ disulfide bond, which we found to be critical for the CD98–IL1RAP interaction. Because the same $CD98^{C109}$ residue is also required for CD98–xCT interactions (17), and because this residue cannot form a disulfide bond with both IL1RAP and xCT simultaneously, we speculate that CD98 binds IL1RAP and xCT separately. Thus, two CD98 molecules may be required to form a functional CD98–IL1RAP–xCT complex. The presence of IL1RAP in this modified system Xc^- complex then augments the activity of the transporter, although additional studies are needed to pinpoint the exact structure and stoichiometry of this protein complex. As to how IL1RAP might affect xCT transporter activity, the latter is a highly regulated process (46, 47). For example, xCT posttranslational modifications (PTM) such as serine-26 phosphorylation by mTORC2 decrease xCT activity without altering its expression level (46, 47). IL1RAP–xCT interactions may therefore alter xCT PTMs by affecting its association with other regulatory molecules, thereby enhancing its transporter activity or efficiency.

Oncoproteins such as mutant KRAS and tumor suppressors such as p53 and BAP1 can activate or repress xCT, respectively, during tumorigenesis (36, 48, 49). Expression of xCT is implicated in oncogenesis in different tumor types, including triple-negative breast cancer, glioblastoma, and non–small cell lung cancer (NSCLC; refs. 50–52). However, when extracellular cystine levels become limited, cells are thought to activate the TSS pathway for *de novo* cysteine synthesis (18). The TSS pathway is physiologically important, as depletion of the key TSS enzyme *Cth* in mice causes systemic vulnerability to oxidative injury, and neurodegeneration resulting from heightened oxidative stress (53, 54). In cancer, cystine can be a limiting nutrient within interstitial fluids (44), which may render tumor cells susceptible to oxidative stress if TSS activity is insufficient. We show that oncogenic EWS–ETS fusion proteins maintain cysteine availability by transcriptionally activating *IL1RAP* to support both arms of cysteine homeostasis. Blocking either IL1RAP-mediated xCT activation, or CTH induction under cystine deprivation, both blunt cysteine acquisition and replenishment in Ewing sarcoma cells, leading to severe GSH depletion and potentially lethal oxidative stress, although exactly how IL1RAP toggles between two arms of cysteine homeostasis mechanistically remains to be determined. Therefore, like $KRAS^{G12V}$ and ETV6–NTRK3, EWS–ETS oncoproteins also induce IL1RAP expression to preserve redox homeostasis.

Although our studies in Ewing sarcoma and studies by others in neuroblastoma (ref. 18; both tumors of which are of neuroectodermal origin) point to an important role for TSS in cysteine replenishment, several studies have reported that TSS does not play a major role in epithelial malignancies such as NSCLC (55). Consistent with this notion, Ewing sarcoma cells are highly sensitive to GSH depletion when treated with the GCL inhibitor BSO, particularly under 3-D growth conditions (Supplementary Fig. S3G–S3I), in contrast to the insensitivity of various epithelial tumor types to BSO, including NSCLC (33). Thus, due to the hypersensitivity of Ewing sarcoma cells to GSH depletion, these cells likely rely on TSS to replenish GSH pools when extracellular cystine becomes transiently depleted, to preserve cell viability. Indeed, we observed a dramatic increase in the expression of TSS enzymes CTH and CBS when cystine uptake was blocked in Ewing sarcoma cells (Supplementary Fig. S6A). We postulate that, as long as TSS substrates are available, TSS is transiently and contextually activated by IL1RAP specifically when extracellular cystine levels become critically low, particularly given the reliance of Ewing sarcoma cells on GSH production from cysteine for redox homeostasis. Although it remains unknown exactly when during the metastatic cascade such a dependence on TSS occurs, it is clear from our *in vivo* studies that both IL1RAP and CTH induction by IL1RAP are critical for metastasis, credentializing IL1RAP as a promising target in Ewing sarcoma. As mentioned above, Ewing sarcoma and other neuroectodermally derived tumors might be unique among human tumors in requiring both cystine uptake through xCT and *de novo* cysteine synthesis for maintaining redox homeostasis. It will be important to test if other human cancers with high IL1RAP expression, such as acute myeloid leukemia, melanoma, and head and neck tumors (Fig. 2A; Supplementary Fig. S2A and S2B), also utilize IL1RAP for xCT and TSS activation, but this requires additional studies.

A recent study reported that high xCT expression and cystine uptake increases consumption of cellular NADPH during cystine-to-cysteine conversion, which can induce redox collapse and cell death under glucose deprivation (20). In contrast, we found that Ewing sarcoma cells are not high xCT expressors compared with other cancers such as lung adenocarcinomas (see Supplementary Fig. S2C). Given the overall detrimental effects of cystine deprivation in Ewing sarcoma cells, e.g., by depleting cystine in the culture media, erastin treatment, or depletion of *IL1RAP* or *CTH*, we posit that the cytoprotective functions of the IL1RAP–xCT–CD98 complex prevail over its potential liabilities, at least under the conditions we tested. Moreover, our experimental conditions are pathologically relevant, as they mimic cystine limitation in the tumor microenvironment (44), or that occur during loss of attachment during the metastatic cascade (4). It is tempting to speculate that tumors with lower levels of xCT expression such as Ewing sarcoma require IL1RAP or other mechanisms to augment xCT activity to preserve cysteine pools and redox balance.

We observed strong immunoreactivity for IL1RAP in the placenta, mirroring a recent finding that extravillous trophoblasts (EVT) of the placenta express high levels of *IL1RAP* mRNA (56). Intriguingly, several features of cancer cells are highly reminiscent of EVTs, such as their capacity to invade and grow into surrounding tissues, similar to invasion of decidualized uterine tissues by ETVs (56). This suggests that IL1RAP may be exploited by both metastatic cancer cells and ETVs to drive invasive capacity. Strikingly, apart from placenta, minimal expression of IL1RAP was observed across a wide spectrum of normal tissues, both pediatric and adult, as well as healthy cord blood and adult blood samples. This nominates IL1RAP, a surface protein, as a potential immunotherapeutic target in Ewing sarcoma. Given the high dependency of Ewing sarcoma cells on IL1RAP-mediated cysteine metabolism for survival under stress, IL1RAP, either alone or in complex with CD98/xCT, is an exploitable vulnerability for cancer therapy in a highly metastatic disease such as Ewing sarcoma. Indeed, biopanning against phage-displayed libraries identified a series of IL1RAP binders, one of which, when used to generate a fully human anti-IL1RAP antibody, showed strong ADCC activity against Ewing sarcoma. Because this antibody is rapidly internalized once bound to Ewing sarcoma cells, future studies are warranted for testing this reagent as an antibody–drug conjugate or, alternatively, for generation of CAR T cells targeting IL1RAP, as therapeutic approaches for Ewing sarcoma. Moreover, our results show that diverse oncogenes, including *ETV6–NTRK3*, *KRAS*^{G12V}, and *EWS–ETS* fusions, activate *IL1RAP* transcription, suggesting that the role of IL1RAP in tumor progression may be broader than anticipated.

METHODS

Cell Culture

NIH3T3, HEK293, HEK293T, and A673 were purchased from ATCC. The CHLA10 Ewing sarcoma cell line was from Dr. Patrick Reynolds (Texas Tech University). TC32 Ewing sarcoma cells were from Dr. Timothy Triche (Children's Hospital Los Angeles). A673 cells expressing Dox-inducible shRNA targeting EWS–FLI1 (sh*EWS–FLI1* TetON) or a negative control shRNA (shCtrl TetON) were kindly provided by Dr. Javier Alonso (Instituto de Investigaciones Biomédicas), and details about these cells were described previously (57). NIH3T3 cells stably expressing the empty vector MSCV, EN, or mutant KRAS^{G12V} were described by our previous studies (58). MSCs L87 and V54.2 were kindly provided by Ralph Huss (Apceth, Munich). NIH3T3 and its derivatives were maintained in DMEM (Sigma) with 10% bovine serum (calf serum, Gibco). A673, HEK293, and HEK293T were cultured in DMEM with 10% fetal bovine serum (FBS; Gibco). TC32 cells were maintained in RPMI 1640 (Sigma) with 10% FBS. CHLA10 were cultured in Iscove's Modified Dulbecco's Medium (Gibco) with 20% FBS plus 1X ITS (Gibco). All media were supplemented with 1% antibiotic-antimycotic (Gibco), and all cells were cultured at 37°C with 5% CO_2. 3-D cultures were performed by plating cells in ultra-low attachment plates, including 6-well, 24-well, and 100-mm plates (Corning), and normal cell growth media were used. All cell lines were tested for *Mycoplasma* on a regular basis using the LookOut Mycoplasma Detection Kit (Sigma). Cell lines were authenticated via short tandem repeat testing, and experiments were performed with the cell lines within 15 to 20 passages from thawing.

Animal Studies

The animal studies were approved by the University of British Columbia Animal Care Committee under the certificate #A10-0200. A well-established murine renal subcapsular implantation model (5, 27) was used to study different stages of Ewing sarcoma progression in mice, including primary tumor growth, local invasion, and distant metastasis. Detailed procedures were described in our previous work (5, 27). Briefly, TC32 cells to be implanted were trypsinized, and single-cell suspension was obtained by passing through 40-µm cell strainers before cell counting. Then, cell blocks were made by mixing the cells with rat tail collagen gel. After 30 minutes incubation at 37°C, the solidified cell blocks were used for implantation in the renal capsules of 6- to 8-week-old male NSG mice (7–10/group). 1×10^6 cells/mouse were used for the IL1RAP studies, and 8×10^5 cells/mouse were used for the CTH studies. Specifically, a 5-mm incision was made to exteriorize the kidney, which was then placed on the body wall. An incision of 2–4 mm in length was made in the kidney capsule, and a Ewing sarcoma cell block was inserted into the subcapsular space. Then, the kidney was eased back into the body cavity, and the skin wound was sutured closed. Animals were maintained in compliance with the University of British Columbia Animal Care Committee regulations. Experimental mice were continuously monitored for approximately five weeks before they were euthanized. Histopathologic and biochemical analyses of the specimens from the animal studies are described in the Supplementary Methods.

Immunoblotting Analysis

Immunoblotting analysis was performed using standard protocols. To determine the expression of small-molecule proteins under 20 kDa, such as cleaved caspase-3, NuPAGE 4%–12% Bis–Tris gels (Invitrogen) were used. Otherwise, 10% or 12% SDS-PAGE gels were used. 10–30 µg of protein lysates were loaded per well, and nitrocellulose membranes (Bio-Rad) were used during protein transfer. Information about the primary antibodies used in immunoblotting is shown in Supplementary Table S3. Horseradish peroxidase (HRP)–conjugated secondary antibodies were used, including goat anti-rabbit IgG (Cell Signaling Technology), goat anti-mouse IgG (Cell Signaling Technology), and donkey anti-goat (Santa Cruz). Membranes were developed using Pierce ECL Western Blotting Substrate or SuperSignal West Pico PLUS Chemiluminescent Substrate (both from Thermo Scientific). Images were acquired by photographic films or the ImageQuant LAS4000 Luminescent Image Analyzer (GE).

Surface IL1RAP Detection by Flow Cytometry

A673 cells were dissociated with CellStripper reagent (Corning), and all other cell types were gently dissociated with 0.25% trypsin-EDTA (Gibco). The dissociation reagents were neutralized with normal growth media. Then, the cells were washed in cold phosphate-buffered saline (PBS) once, and 1×10^6 cells/100 µL were stained with a PE-conjugated IL1RAP antibody (R&D Systems, FAB676P) or an APC-conjugated IL1RAP antibody (R&D Systems, FAB676A) in HBSS-2% FBS buffer in the dark for 30 minutes on ice. Nonstained or isotype control antibody-stained cells were used as negative controls. After washing in cold PBS once, cells were analyzed using BD FACSCalibur flow cytometer. FL-2 channel (IL1RAP–PE) or FL-4 channel (IL1RAP–APC) was used during data collection, and 10,000 events were analyzed per condition. FlowJo v10 (FlowJo LLC) software was used to analyze median fluorescence intensities.

To determine IL1RAP protein expression in hematopoietic cells, anonymized consented heparinized samples of normal cord blood cells were obtained with written informed consent according to University of British Columbia Research Ethics Board–approved protocols. Peripheral blood was also collected from healthy adult volunteers with written informed consent and anonymized. Blood was then blocked in PBS + 5% human serum + 0.5% anti-human CD32 antibody clone IV.3 (0.5 mg/mL, all from STEMCELL Technologies) and stained with CD33-PECF594 (BD Horizon, 562492), CD19-APC-ef780 (Invitrogen, 47-0198-42), CD3-SB600 (Invitrogen, 63-0037-42), CD15-PECy7 (BD Pharmingen, 560827), CD14-FITC (STEMCELL Technologies, 60124FI), CD34-AF647 (BioLegend, 343508) and either IL1RAP–PE (R&D Systems, FAB676P) or an IgG1-PE isotype control (R&D Systems, IC002P). Red blood cells were then lysed in a 4% ammonium chloride solution (STEMCELL Technologies), then samples were washed and centrifuged (5 minutes, 300 × *g*) prior to resuspension in a 0.1% propidium iodide solution (1 mg/mL, Sigma-Aldrich) for analysis on a BD FACSymphony.

General ROS and Lipid ROS Detection

General oxidative stress indicator CM-H2-DCFDA (0.1 mmol/L, Molecular Probes) or CellROX Deep Red Reagent (1:500, Molecular Probes) was used to measure cellular ROS levels. Lipid ROS was detected by staining cells with lipid peroxidation sensor BODIPY 581/591 C11 (2 μmol/L, Molecular Probes). Briefly, cells grown in 2-D adherent conditions or 3-D cultures (48–72 hours for Ewing sarcoma cells) were dissociated with CellStripper (A673 cells) or 0.25% trypsin-EDTA (all other cell lines), and the cells were resuspended in normal growth media containing those reagents or DMSO (as a negative control). The samples were incubated for 30 minutes (lipid ROS) or 45 minutes (general ROS) at 37°C. Then, cells were washed, resuspended in cold PBS, and analyzed on a BD FACSCalibur flow cytometer by FL-1 channel (CM-H2-DCFDA and BODIPY 581/591 C11) or FL-4 channel (CellROX Deep Red). Data were analyzed using FlowJo v10 (FlowJo LLC), and the percentage of lipid ROS-high cells (arbitrary based on the intensity of controls) and median fluorescence intensity of general ROS were assessed.

^{13}C-Serine Metabolic Flux and Analysis of ^{12}C- and ^{13}C-Labeled Thiol Compounds

Cell lines were plated in 6-well plates, 5×10^5 cells/well, and the cells were allowed to attach for 48 hours. To measure *de novo* cysteine synthesis, the cells were cultured in cystine- and serine-free DMEM (USBiological) supplemented with 400 μmol/L [3-^{13}C] L-Serine (Cambridge Isotope Laboratories) and 10% dialyzed FBS (Gibco). Because it has been shown that cysteine is rapidly metabolized to GSH under cystine-deprivation and high ROS conditions (37), we used a protocol recently published by the Thompson laboratory to effectively trace newly synthesized cysteine production (18). Specifically, to maintain redox homeostasis under cystine limitation during the course of the experiment, 50 μmol/L 2-mercaptoethanol was added in the media. Cells were collected after 24 hours in cold 80:20 methanol:water and kept at −80°C before analysis. On the day of analysis, the cell pellets were resuspended in 250 μL of 70% acetonitrile, and the metabolites were extracted by homogenization as described above. Ten serially diluted standard solutions were prepared in 70% acetonitrile and in a concentration range of 0.0002 to 10 μmol/L. Supernatant (20 μL) of each sample solution or each standard solution was mixed with 180 μL of 20 mmol/L N-ethylmaleimide solution. After vortex mixing, 10 μL aliquots of each resultant solution were injected to run UPLC-MRM/MS on an Agilent 1290 UHPLC system coupled to an Agilent 6495B triple-quadrupole mass spectrometer operated in the positive-ion mode. LC separation was carried out on a polar reverse-phase C18 column (2.1 × 100 mm, 2 μm) with the use of 0.1% formic acid in water and 0.1% formic acid in methanol as the binary solvents for gradient elution (2%–40% B in 12 minutes) at 45°C and 0.3 mL/min. Concentrations of the detected compounds were calculated with the analyte peak areas measured from the sample solutions by interpolating the constructed linear-regression curves of individual compounds. The percentages of 13C mass isotopomers of each compound were calculated by dividing the peak areas of its 13C mass isotopomers by the peak area of its monoisotopic ion, both of which were measured in each of the same sample solutions. The percentages were then corrected with the natural 13C distribution abundances of individual mass isotopomers of each compound, which were calculated from injections of the standard solutions.

ChIP-qPCR

The Magna ChIP HiSens (Millipore) kit was used for ChIP analysis following the manufacturer's protocol. In brief, A673 shEWS–FLI1 TetON cells plated in 15-cm plates were treated with/without 500 nmol/L Dox for 72 hours. Chromatin cross-linking was performed by fixing the cells with 1% formaldehyde for 10 minutes at room temperature. Then, the cross-linked chromatin was sheared to ~200 bp–1,000 bp fragments using a sonicator (Model CPX130PB, Cole-Parmer). The sheared chromatin samples were immunoprecipitated with the following antibodies overnight at 4°C: FLI1 antibody (1:100, ab15289, Abcam), SMARCC1/BAF155 antibody (1:100, #11956, Cell Signaling Technology), p300 antibody (1:50, #54062, CST), H3K27ac antibody (1:100, #39133, Active Motif), or normal rabbit IgG (5 μg/mL, #2729, Cell Signaling Technology). Subsequent qPCR analysis was performed using Fast SYBR Green Master Mix (Applied Biosystems) in a QuantStudio 6 Real-Time PCR Systems instrument (Thermo Fisher). The primers used for ChIP-qPCR are described in Supplementary Table S4. For qPCR analysis, the comparative C_t method was used to quantify the relative level of each target by normalization to the input control.

Coimmunoprecipitation (co-IP) and IL1RAP Interactome Analysis

Cell Lysate Preparation. CelLytic M buffer (Sigma) supplemented with protease inhibitors and phosphatase inhibitors were used to prepare cell lysates for co-IP. For regular co-IP experiments that aim to determine protein–protein interactions by immunoblotting, cells were washed with cold PBS and directly lysed in CelLytic M buffer by pipetting up and down every 5 minutes for 30 minutes on ice. For IL1RAP interactome analysis, formaldehyde cross-linking was performed before co-IP. Briefly, A673 cells grown at ~90% confluence were washed with PBS twice before being incubated with 2% formaldehyde diluted in PBS for 10 minutes (5 minutes incubation and 5 minutes handling time for pelleting cells by centrifugation) at room temperature. The cross-linking was terminated by adding ice-cold 1.25M glycine in PBS to the cell pellets. After washing the cells again with ice-cold 1.25M glycine, the cells were lysed in CelLytic M buffer as described above. The cell lysates were centrifuged at 12,000 × *g* for 10 minutes, and the supernatant was collected.

Co-IP. Protein concentrations were determined by the BCA protein assay (Thermo Fisher), and 0.5–1.0 mg of cell lysates in the volume of 500 μL was used for each co-IP reaction. Specifically, primary antibodies were incubated with cell lysates overnight with rotation at 4°C. For DTT treatment, 10 mmol/L (final) was added to the lysates at this step. The amount of antibody/reaction was: 2 μg for goat anti-IL1RAP (AF676, R&D Systems) and normal goat IgG control (AB-108-C, R&D Systems), 1:50 for rabbit anti-HA tag (#3724, Cell Signaling Technology), 1:50 for rabbit anti-xCT (#12691, Cell Signaling Technology), and 1:200 for rabbit anti-CD98 (H00006520-D01P, Novus Biologicals). Then, 50 µL Dynabeads Protein G (Thermo Fisher) was added to each reaction and incubated for 60 minutes with rotation at room temperature. After that, the beads were washed four times with cold CelLytic M buffer. For subsequent immunoblotting analysis, the beads were resuspended in 30–50 µL 2× SDS gel loading buffer and boiled at 95°C for 5 minutes to elute proteins. For IL1RAP interactome analysis by mass spectrometry, the purified proteins were subjected to trypsin digestion (Promega, V5073, 1:50 µg:µg trypsin to protein) directly on the Dynabeads in 100 mmol/L ammonium bicarbonate at 37°C for 18 hours with mixing at 1,000 rpm in a thermomixer. The MS settings for IL1RAP interactome analysis are described in the Supplementary Methods.

PLA

PLA in Cell Lines. To evaluate *in situ* protein interactions in cell lines, PLA was performed following the manufacturer's instructions (Duolink *In Situ* Red Starter Kit Mouse/Rabbit, Duo92101, Sigma-Aldrich). Specifically, cells grown on chamber slides (Millipore) were fixed in 4% paraformaldehyde for 10 minutes at room temperature. After rinsing with PBS 3 times, cells were permeabilized in 0.2% Triton X-100 in PBS for 10 minutes at room temperature (this step was omitted for IL1RAP–xCT PLA). After rinsing with PBS 3 times, cells were blocked in blocking buffer supplied in the kit, and incubated for 1.5 hours with primary antibodies against IL1RAP (1:100, mouse anti-IL1RAP, MAB676, R&D Systems) and rabbit anti-CD98 (1:200, H00006520-D01P, Novus Biologicals), or rabbit anti-HA (1:500, #3724, Cell Signaling Technology), or rabbit anti-xCT (1:500, NB300-317, Novus Biologicals). Negative controls were incubated with a single antibody or no primary antibody. Nuclei were counterstained with DAPI within the mounting medium supplied by the kit. Manufacturer's instructions were followed for all additional procedures of the assay. Fluorescent images were taken on an LSM Airyscan 800 confocal microscope using a 63x oil immersion objective and the Zen Blue software (Zeiss). PLA fluorescent intensities were quantified using ImageJ v1.52q (NIH) on 5–7 images with >20 cells/image. Mean fluorescence per cell was calculated and compared among different groups.

PLA in Formalin-Fixed Paraffin-Embedded Tissues. To assess endogenous protein interactions between IL1RAP–CD98 and IL1RAP–xCT, PLA was conducted in formalin-fixed, paraffin-embedded (FFPE) tissues using Duolink PLA Brightfield Detection (Sigma-Aldrich). Briefly, Ewing sarcoma xenograft tissue samples were assessed for IL1RAP–CD98 and IL1RAP–xCT interactions using the Ventana DISCOVERY Ultra autostainer (Ventana Medical Systems). Baked and deparaffinized FFPE tissue sections were incubated in Tris-based buffer (CC1, Ventana) at 95°C for 64 minutes for antigen retrieval, followed by incubation at room temperature for 12 hours with the following primary antibody cocktail solution (prepared in 1 × TBS diluent): IL1RAP (1:25, R&D Systems, goat polyclonal, #AF676) with either CD98 (1:25, rabbit monoclonal, Cell Signaling Technology, #94274) or xCT (1:200, rabbit polyclonal, NB300-317, Novus Biologicals), respectively. Subsequent PLA procedures were performed according to the manufacturer's protocol with the following modifications adapted for the Ventana autostainer: prepared solutions were doubled in concentration from the manufacturer's protocol except for PLA probes; all reagents were prepared using double-distilled water as diluent; all wash steps used 1 × Reaction Buffer (Ventana); amplification was conducted at 37°C for 4 hours; tissue was counterstained with Ventana hematoxylin and bluing reagent; and tissue was further washed to remove liquid coverslip prior to slide mounting. Images were acquired with the fixed-stage upright BX51W1 microscope (Olympus). If protein targets are close (<40 nm apart), the appending PLA probes hybridize and ligate to form a circular template, which is then amplified. The amplicon (linked to protein targets) is visualized using complementary oligonucleotide detection probes and substrates, producing discrete dots as a readout of localized protein interactions.

IF Analysis

Cells grown on chamber slides (Millipore) were fixed in 4% paraformaldehyde for 10 minutes at room temperature, and rinsed three times in PBS between each of the following steps. Cells were permeabilized with 0.2% Triton X-100 in PBS for 10 minutes at room temperature (this step was omitted for surface xCT staining) and blocked with 5% BSA in PBS for 1 hour. Then, cells were incubated at room temperature for 1 hour with primary antibodies against IL1RAP (1:200, AF676, R&D Systems) and/or CD98 (1:200, H00006520-D01P, Novus Biologicals), and/or HA-tag (1:500, #3724, Cell Signaling Technology), and/or xCT (1:500, NB300-317, Novus Biologicals). Cells were subsequently incubated at room temperature for 1 hour with respective IgG (H + L) secondary antibodies conjugated with Alexa Fluor 488, Alexa Fluor 568, and/or Alexa Fluor 594 (Molecular Probes, all 1:300). All antibodies were diluted in 5% BSA in PBS. Then, cells were rinsed with PBS three times, and nuclei were counterstained with DAPI within the VECTASHIELD Hardset Antifade Mounting Medium (Vector Laboratories). The images were taken on an LSM Airyscan 800 confocal microscope using a 63× oil immersion objective and the Zen Blue software (Zeiss).

IL1RAP V_H Binder Identification and Conversion into V_H–Fc

To identify anti-IL1RAP antibodies, a human immunoglobulin G heavy-chain variable domain (V_H) phage-displayed library (59) was used for panning against the IL1RAP ectodomain (SinoBiological, 10121-H08H). The recombinant IL1RAP protein was biotinylated through the amine coupling by using EZ-Link NHS-PEG4-Biotin reagents (Thermo Fisher, 21330). The panning was performed for three rounds with input antigens of 10, 2, and 0.5 µg for the first, second, and third rounds, respectively. Approximately 1×10^{12} V_H phage particles were incubated with biotinylated IL1RAP followed by washing with PBS containing 0.1% Tween-20. Bound phage pulled down by streptavidin-M280-Dynabeads (Thermo Fisher, 11205D) was rescued by log-phase TG1 cells under the help of the M13KO7 helper phage (Thermo Fisher, 18311019). After three rounds of panning, positive clones were selected by soluble expression monoclonal (SEM) ELISA followed by Sanger sequencing. V_H binders were further validated for their binding affinity by ELISA and cell binding by flow cytometry. For conversion to the Fc fusion, the V_H gene was subcloned into pSecTag B vector containing an in-frame human IgG1 Fc fragment. The V_H–Fc protein was expressed in expi293 cells by transient transfection and purified by protein A resin.

Quantification and Statistical Analysis

Statistical details of MS data analysis are described separately in the section devoted to this type of data acquisition. GraphPad Prism software (version 7 or 8) was used for all other statistical analyses. Student unpaired t tests (two-tailed) were used to compare differences between two groups. Log-rank test was used in Kaplan–Meier survival analysis. For all statistical analyses; n.s., nonsignificant; *, $P < 0.05$; **, $P < 0.01$; ***, $P < 0.001$. Otherwise indicated in the figure legends, all data presented are means ± SD.

Data Availability

All mass spectrometry proteomics data in this study have been deposited to the ProteomeXchange Consortium via the PRIDE (60) partner repository with the data set identifier PXD019009. The data sets include proteomic and acute translatomic analysis in NIH3T3 cells stably expressing MSCV vector control, $KRAS^{G12V}$, or ETV6–NTRK3 cultured in 3-D conditions, IL1RAP interactome analysis in A673 cells, and proteomic analysis in A673 cells in 3-D cultures with control knockdown or *IL1RAP* knockdown by shRNA #39 or #40. The repository contains raw data, search results, detailed MS acquisition method parameters, and TMT labeling schemes for all proteomic analyses performed in this work. All other relevant data are available from the corresponding author on reasonable request.

Other methods used in this study are described in the Supplementary Methods.

Authors' Disclosures

R.J. Orentas, D.S. Dimitrov, L. Wei, H.-F. Zhang, and P.H. Sorensen have filed a patent for IL1RAP CAR-T constructs (PCT/US2021/026727). R.J. Orentas, D.S. Dimitrov, and P.H. Sorensen report grants from NIH, St. Baldrick's Foundation/Stand Up To Cancer/AACR. In addition, R.J. Orentas reports consulting fees from Umoja Biopharma and research support from Miltenyi Biotec. No disclosures were reported by the other authors.

Authors' Contributions

H.-F. Zhang: Conceptualization, data curation, formal analysis, methodology, writing–original draft. **C.S. Hughes:** Formal analysis, methodology, writing–review and editing. **W. Li:** Resources, data curation. **J.-Z. He:** Data curation. **D. Surdez:** Data curation. **A.M. El-Naggar:** Data curation and formal analysis. **H. Cheng:** Methodology. **A. Prudova:** Data curation. **A. Delaidelli:** Data curation. **G.L. Negri:** Formal analysis. **X. Li:** Data curation. **M.S. Ørum-Madsen:** Methodology. **M.M. Lizardo:** Methodology. **H.Z. Oo:** Data curation. **S. Colborne:** Formal analysis. **T. Shyp:** Data curation. **R. Scopim-Ribeiro:** Data curation. **C.A. Hammond:** Data curation. **A.-C. Dhez:** Formal analysis. **S. Langman:** Methodology. **J.J.K. Lim:** Resources. **S.H.Y. Kung:** Visualization. **A. Li:** Project administration. **A. Steino:** Project administration. **M. Daugaard:** Resources. **S.J. Parker:** Writing–review and editing. **R.I. Klein Geltink:** Writing–review and editing. **R.J. Orentas:** Resources. **L.-Y. Xu:** Resources. **G.B. Morin:** Methodology. **O. Delattre:** Resources. **D.S. Dimitrov:** Resources. **P.H. Sorensen:** Conceptualization, supervision, funding acquisition, writing–review and editing.

Acknowledgments

We thank Drs. Xin Jiang, Khushbu Patel, Tianqing Yang, and Joe Yuezhou Huang, Jordan Cran, Sylvia Lee, and Rebecca Wu for technical assistance, and the Sorensen laboratory members for helpful discussions. We thank the Flow Cytometry Core and Animal Resource Centre at BC Cancer Research Centre. We thank the funding support from the NIH U54 Pediatric Immunotherapy Discovery and Development Network (1U54CA232568-01), a St. Baldrick's Foundation/American Association for Cancer Research/Stand Up To Cancer Pediatric Dream Team Translational Research Grant (SU2C-AACR-DT-27-17), and a St. Baldrick's Foundation/Martha's Better Ewing Sarcoma Treatment (BEST) Grant (#663113). Stand Up To Cancer (SU2C) is a division of the Entertainment Industry Foundation, and research grants are administered by the American Association for Cancer Research, the scientific partner of SU2C. The content is solely the responsibility of the authors and does not necessarily represent the official views of the NIH. H.-F. Zhang is funded by a fellowship from the Canadian Institutes of Health Research (#415377) and a trainee award from the Michael Smith Foundation for Health Research partnered with the Lotte and John Hecht Memorial Foundation (#18569).

The publication costs of this article were defrayed in part by the payment of publication fees. Therefore, and solely to indicate this fact, this article is hereby marked "advertisement" in accordance with 18 USC section 1734.

Note

Supplementary data for this article are available at Cancer Discovery Online (http://cancerdiscovery.aacrjournals.org/).

Received November 21, 2020; revised April 3, 2021; accepted May 13, 2021; published first May 21, 2021.

REFERENCES

1. Lambert AW, Pattabiraman DR, Weinberg RA. Emerging biological principles of metastasis. Cell 2017;168:670–91.
2. Steeg PS. Targeting metastasis. Nat Rev Cancer 2016;16:201–18.
3. Grünewald TGP, Cidre-Aranaz F, Surdez D, Tomazou EM, de Álava E, Kovar H, et al. Ewing sarcoma. Nat Rev Dis Primers 2018;4:5.
4. Buchheit CL, Weigel KJ, Schafer ZT. Cancer cell survival during detachment from the ECM: multiple barriers to tumour progression. Nat Rev Cancer 2014;14:632–41.
5. Mendoza-Naranjo A, El-Naggar A, Wai DH, Mistry P, Lazic N, Ayala FR, et al. ERBB4 confers metastatic capacity in Ewing sarcoma. EMBO Mol Med 2013;5:1087–102.
6. Wang T, Wei JJ, Sabatini DM, Lander ES. Genetic screens in human cells using the CRISPR-Cas9 system. Science 2014;343:80–4.
7. Shalem O, Sanjana NE, Hartenian E, Shi X, Scott DA, Mikkelson T, et al. Genome-scale CRISPR-Cas9 knockout screening in human cells. Science 2014;343:84–7.
8. Meyers RM, Bryan JG, McFarland JM, Weir BA, Sizemore AE, Xu H, et al. Computational correction of copy number effect improves specificity of CRISPR-Cas9 essentiality screens in cancer cells. Nat Genet 2017;49:1779–84.
9. Rotem A, Janzer A, Izar B, Ji Z, Doench JG, Garraway LA, et al. Alternative to the soft-agar assay that permits high-throughput drug and genetic screens for cellular transformation. Proc Natl Acad Sci U S A 2015;112:5708–13.
10. Lu SC. Regulation of glutathione synthesis. Mol Aspects Med 2009;30:42–59.
11. Combs JA, DeNicola GM. The non-essential amino acid cysteine becomes essential for tumor proliferation and survival. Cancers 2019;11:678.
12. Schafer ZT, Grassian AR, Song L, Jiang Z, Gerhart-Hines Z, Irie HY, et al. Antioxidant and oncogene rescue of metabolic defects caused by loss of matrix attachment. Nature 2009;461:109–13.
13. Jiang L, Shestov AA, Swain P, Yang C, Parker SJ, Wang QA, et al. Reductive carboxylation supports redox homeostasis during anchorage-independent growth. Nature 2016;532:255–8.
14. Dixon SJ, Lemberg KM, Lamprecht MR, Skouta R, Zaitsev EM, Gleason CE, et al. Ferroptosis: an iron-dependent form of nonapoptotic cell death. Cell 2012;149:1060–72.
15. Stockwell BR, Friedmann Angeli JP, Bayir H, Bush AI, Conrad M, Dixon SJ, et al. Ferroptosis: a regulated cell death nexus linking metabolism, redox biology, and disease. Cell 2017;171:273–85.
16. Badgley MA, Kremer DM, Maurer HC, DelGiorno KE, Lee HJ, Purohit V, et al. Cysteine depletion induces pancreatic tumor ferroptosis in mice. Science 2020;368:85–9.
17. Conrad M, Sato H. The oxidative stress-inducible cystine/glutamate antiporter, system x (c) (-): cystine supplier and beyond. Amino Acids 2012;42:231–46.
18. Zhu J, Berisa M, Schwörer S, Qin W, Cross JR, Thompson CB. Transsulfuration activity can support cell growth upon extracellular cysteine limitation. Cell Metab 2019;30:865–76.
19. Doll S, Freitas FP, Shah R, Aldrovandi M, da Silva MC, Ingold I, et al. FSP1 is a glutathione-independent ferroptosis suppressor. Nature 2019;575:693–8.
20. Liu X, Olszewski K, Zhang Y, Lim EW, Shi J, Zhang X, et al. Cystine transporter regulation of pentose phosphate pathway dependency and disulfide stress exposes a targetable metabolic vulnerability in cancer. Nat Cell Biol 2020;22:476–86.
21. Boraschi D, Tagliabue A. The interleukin-1 receptor family. Semin Immunol 2013;25:394–407.
22. Järås M, Johnels P, Hansen N, Agerstam H, Tsapogas P, Rissler M, et al. Isolation and killing of candidate chronic myeloid leukemia stem cells by antibody targeting of IL-1 receptor accessory protein. Proc Natl Acad Sci U S A 2010;107:16280–5.

23. Barreyro L, Will B, Bartholdy B, Zhou L, Todorova TI, Stanley RF, et al. Overexpression of IL-1 receptor accessory protein in stem and progenitor cells and outcome correlation in AML and MDS. Blood 2012;120:1290–8.
24. Ågerstam H, Karlsson C, Hansen N, Sandén C, Askmyr M, von Palffy S, et al. Antibodies targeting human IL1RAP (IL1R3) show therapeutic effects in xenograft models of acute myeloid leukemia. Proc Natl Acad Sci U S A 2015;112:10786–91.
25. Mitchell K, Barreyro L, Todorova TI, Taylor SJ, Antony-Debré I, Narayanagari SR, et al. IL1RAP potentiates multiple oncogenic signaling pathways in AML. J Exp Med 2018;215:1709–27.
26. Tirode F, Laud-Duval K, Prieur A, Delorme B, Charbord P, Delattre O. Mesenchymal stem cell features of Ewing tumors. Cancer Cell 2007; 11:421–9.
27. El-Naggar AM, Veinotte CJ, Cheng H, Grunewald TG, Negri GL, Somasekharan SP, et al. Translational activation of HIF1α by YB-1 promotes sarcoma metastasis. Cancer Cell 2015;27:682–97.
28. El-Naggar AM, Somasekharan SP, Wang Y, Cheng H, Negri GL, Pan M, et al. Class I HDAC inhibitors enhance YB-1 acetylation and oxidative stress to block sarcoma metastasis. EMBO Rep 2019;20:e48375.
29. Piskounova E, Agathocleous M, Murphy MM, Hu Z, Huddlestun SE, Zhao Z, et al. Oxidative stress inhibits distant metastasis by human melanoma cells. Nature 2015;527:186–91.
30. Wiel C, Le Gal K, Ibrahim MX, Jahangir CA, Kashif M, Yao H, et al. BACH1 stabilization by antioxidants stimulates lung cancer metastasis. Cell 2019;178:330–45.
31. Tasdogan A, Faubert B, Ramesh V, Ubellacker JM, Shen B, Solmonson A, et al. Metabolic heterogeneity confers differences in melanoma metastatic potential. Nature 2020;577:115–20.
32. Griffith OW, Meister A. Potent and specific inhibition of glutathione synthesis by buthionine sulfoximine (S-n-butyl homocysteine sulfoximine). J Biol Chem 1979;254:7558–60.
33. Harris IS, Endress JE, Coloff JL, Selfors LM, McBrayer SK, Rosenbluth JM, et al. Deubiquitinases maintain protein homeostasis and survival of cancer cells upon glutathione depletion. Cell Metab 2019;29: 1166–81.
34. Shin CS, Mishra P, Watrous JD, Carelli V, D'Aurelio M, Jain M, et al. The glutamate/cystine xCT antiporter antagonizes glutamine metabolism and reduces nutrient flexibility. Nat Commun 2017;8:15074.
35. Gout PW, Buckley AR, Simms CR, Bruchovsky N. Sulfasalazine, a potent suppressor of lymphoma growth by inhibition of the X(c)-cystine transporter: a new action for an old drug. Leukemia 2001;15: 1633–40.
36. Zhang Y, Shi J, Liu X, Feng L, Gong Z, Koppula P, et al. BAP1 links metabolic regulation of ferroptosis to tumour suppression. Nat Cell Biol 2018;20:1181–92.
37. Kelly B, Carrizo GE, Edwards-Hicks J, Sanin DE, Stanczak MA, Priesnitz C, et al. Sulfur sequestration promotes multicellularity during nutrient limitation. Nature 2021;591:471–6.
38. Szabó C. Hydrogen sulphide and its therapeutic potential. Nat Rev Drug Discov 2007;6:917–35.
39. Riggi N, Knoechel B, Gillespie SM, Rheinbay E, Boulay G, Suvà ML, et al. EWS–FLI1 utilizes divergent chromatin remodeling mechanisms to directly activate or repress enhancer elements in Ewing sarcoma. Cancer Cell 2014;26:668–81.
40. Boulay G, Sandoval GJ, Riggi N, Iyer S, Buisson R, Naigles B, et al. Cancer-specific retargeting of BAF complexes by a prion-like domain. Cell 2017;171:163–78.
41. Guillon N, Tirode F, Boeva V, Zynovyev A, Barillot E, Delattre O. The oncogenic EWS–FLI1 protein binds in vivo GGAA microsatellite sequences with potential transcriptional activation function. PLoS One 2009;4:e4932.
42. Gangwal K, Sankar S, Hollenhorst PC, Kinsey M, Haroldsen SC, Shah AA, et al. Microsatellites as EWS/FLI response elements in Ewing's sarcoma. Proc Natl Acad Sci U S A 2008;105:10149–54.
43. Alver BH, Kim KH, Lu P, Wang X, Manchester HE, Wang W, et al. The SWI/SNF chromatin remodelling complex is required for maintenance of lineage specific enhancers. Nat Commun 2017;8: 14648.
44. Sullivan MR, Danai LV, Lewis CA, Chan SH, Gui DY, Kunchok T, et al. Quantification of microenvironmental metabolites in murine cancers reveals determinants of tumor nutrient availability. Elife 2019;8:e44235.
45. Ishimoto T, Nagano O, Yae T, Tamada M, Motohara T, Oshima H, et al. CD44 variant regulates redox status in cancer cells by stabilizing the xCT subunit of system xc(-) and thereby promotes tumor growth. Cancer Cell 2011;19:387–400.
46. Gu Y, Albuquerque CP, Braas D, Zhang W, Villa GR, Bi J, et al. mTORC2 regulates amino acid metabolism in cancer by phosphorylation of the cystine-glutamate antiporter xCT. Mol Cell 2017;67: 128–38.
47. Lien EC, Ghisolfi L, Geck RC, Asara JM, Toker A. Oncogenic PI3K promotes methionine dependency in breast cancer cells through the cystine-glutamate antiporter xCT. Sci Signal 2017;10:eaao6604.
48. Jiang L, Kon N, Li T, Wang SJ, Su T, Hibshoosh H, et al. Ferroptosis as a p53-mediated activity during tumour suppression. Nature 2015;520:57–62.
49. Lim JKM, Delaidelli A, Minaker SW, Zhang HF, Colovic M, Yang H, et al. Cystine/glutamate antiporter xCT (SLC7A11) facilitates oncogenic RAS transformation by preserving intracellular redox balance. Proc Natl Acad Sci U S A 2019;116:9433–42.
50. Timmerman LA, Holton T, Yuneva M, Louie RJ, Padró M, Daemen A, et al. Glutamine sensitivity analysis identifies the xCT antiporter as a common triple-negative breast tumor therapeutic target. Cancer Cell 2013;24:450–65.
51. Tsuchihashi K, Okazaki S, Ohmura M, Ishikawa M, Sampetrean O, Onishi N, et al. The EGF receptor promotes the malignant potential of glioma by regulating amino acid transport system xc(-). Cancer Res 2016;76:2954–63.
52. Ji X, Qian J, Rahman SMJ, Siska PJ, Zou Y, Harris BK, et al. xCT (SLC7A11)-mediated metabolic reprogramming promotes non-small cell lung cancer progression. Oncogene 2018;37:5007–19.
53. Ishii I, Akahoshi N, Yamada H, Nakano S, Izumi T, Suematsu M. Cystathionine gamma-Lyase-deficient mice require dietary cysteine to protect against acute lethal myopathy and oxidative injury. J Biol Chem 2010;285:26358–68.
54. Paul BD, Sbodio JI, Xu R, Vandiver MS, Cha JY, Snowman AM, et al. Cystathionine γ-lyase deficiency mediates neurodegeneration in Huntington's disease. Nature 2014;509:96–100.
55. Kang YP, Mockabee-Macias A, Jiang C, Falzone A, Prieto-Farigua N, Stone E, et al. Non-canonical glutamate-cysteine ligase activity protects against ferroptosis. Cell Metab 2021;33:174–89.
56. Pavličev M, Wagner GP, Chavan AR, Owens K, Maziarz J, Dunn-Fletcher C, et al. Single-cell transcriptomics of the human placenta: inferring the cell communication network of the maternal-fetal interface. Genome Res 2017;27:349–61.
57. Carrillo J, García-Aragoncillo E, Azorín D, Agra N, Sastre A, González-Mediero I, et al. Cholecystokinin down-regulation by RNA interference impairs Ewing tumor growth. Clin. Cancer Res 2007;13: 2429–40.
58. Leprivier G, Remke M, Rotblat B, Dubuc A, Mateo AR, Kool M, et al. The eEF2 kinase confers resistance to nutrient deprivation by blocking translation elongation. Cell 2013;153:1064–79.
59. Li W, Schäfer A, Kulkarni SS, Liu X, Martinez DR, Chen C, et al. High potency of a bivalent human V(H) domain in SARS-CoV-2 animal models. Cell 2020;183:429–41.
60. Perez-Riverol Y, Csordas A, Bai J, Bernal-Llinares M, Hewapathirana S, Kundu DJ, et al. The PRIDE database and related tools and resources in 2019: improving support for quantification data. Nucleic Acids Res 2019;47:D442–50.